Pulsated Global Hydrogen and Methane Flux at Mid-Ocean Ridges Driven by Pangea Breakup

Andrew S. Merdith, Pablo García. del Real, Isabelle Daniel, Muriel Andreani, Nicky M. Wright, Nicolas Coltice

Geochemistry, Geophysics, Geosystems

RESEARCH ARTICLE
10.1029/2019GC008869

Pulsated Global Hydrogen and Methane Flux at Mid-Ocean Ridges Driven by Pangea Breakup

Andrew S. Merdith[1], Pablo García del Real[1,2], Isabelle Daniel[1], Muriel Andreani[1], Nicky M. Wright[3], and Nicolas Coltice[4]

[1]Laboratoire de Géologie de Lyon Terre, Planétes, Environment, Université Lyon 1, Ens de Lyon, CNRS, UMR 5276 LGL-TPE, Villeurbanne, France, [2]Fugro USA Marine, Inc. (FUSAMI), Houston, TX, USA, [3]Research School of Earth Sciences and ARC Centre of Excellence for Climate Extremes, The Australian National University, Canberra, Australia, [4]Laboratoire de Géologie, École Normale Supérieure, CNRS UMR, PSL Research University, Paris, France

Key Points:
- Hydrogen flux from serpentinization reactions, and accompanying methane flux at mid-ocean ridges estimated for the past 200 Ma
- Evolution of slow and ultraslow spreading ridges controls pulses of hydrogen production
- Hydrogen production driven by supercontinent breakup

Correspondence to:
A. S. Merdith,
andrew.merdith@univ-lyon1.fr

Citation:
Merdith, A. S., del Real, P. G., Daniel, I., Andreani, M., Wright, N. M., & Coltice, N. (2020). Pulsated global hydrogen and methane flux at mid-ocean ridges driven by Pangea breakup. *Geochemistry, Geophysics, Geosystems*, *21*, e2019GC008869. https://doi.org/10.1029/2019GC008869

Received 12 DEC 2019
Accepted 16 MAR 2020
Accepted article online 25 MAR 2020

Abstract Molecular hydrogen production occurs through the serpentinization of mantle peridotite exhumed at mid-ocean ridges. Hydrogen is considered essential to sustain microbial life in the subsurface; however, estimates of hydrogen flux through geological time are unknown. Here we present a model of the primary, abiotic production of molecular hydrogen from the serpentinization of oceanic lithosphere using full-plate tectonic reconstructions for the last 200 Ma. We find significant variability in hydrogen fluxes (1–70 • 10^{16} mol/Ma or 0.2–14.1 • 10^{5} Mt/Ma), which are a function of the sensitivity of evolving ocean basins to spreading rates and can be correlated with the opening of key ocean basins during the breakup of Pangea. We suggest that the primary driver of this hydrogen flux is the continental reconfiguration during Pangea breakup, as this produces ocean basins more conducive to exhuming and exposing mantle peridotite at slow and ultraslow spreading ridges. Consequently, present-day flux estimates are ~7 • 10^{17} mol/Ma (1.4 • 10^{6} Mt/Ma), driven primarily by the slow and ultraslow spreading ridges in the Atlantic, Indian, and Arctic oceans. As methane has also been sampled alongside hydrogen at hydrothermal vents, we estimate the methane flux using methane-to-hydrogen ratios from present-day hydrothermal vent fluids. These ratios suggest that methane flux ranges between 10 and 100% of the total hydrogen flux, although as the release of methane from these systems is still poorly understood, we suggest a lower estimate, equivalent to around 7–12 • 10^{16} mol/Ma (1.1–1.9 • 10^{6} Mt/Ma) of methane.

Plain Language Summary Hydrogen gas is produced when mantle rocks are exposed and react with ocean water at slow spreading mid-ocean ridges. Only these ridges tend to expose vast expanses of mantle rocks because the temperature is too cool to generate sufficient melt to produce basaltic oceanic crust. Hydrogen produced in this way is consumed by microbial life; however, there is no record of hydrogen through geological time. To overcome this we built a model approximating the volume of serpentinized mantle rocks produced at slow spreading ridges and used geochemical data to constrain the amount of hydrogen that can be produced, as the Fe (II)/[Fe (II) + Fe (III)] of serpentinite is a proxy of hydrogen production from serpentinization. In order to estimate the flux through time, we use global plate models which trace mid-ocean ridges and the spreading rate. We find that the volume of hydrogen produced is greatest when slow ridges are most abundant and that hydrogen production is concentrated from ridges in the Atlantic, Arctic, and Indian oceans. This is because when a supercontinent breaks up, it produces internal ocean basins that evolve slowly, relative to an ocean basin encompassing the supercontinent (i.e., the Pacific Ocean).

1. Introduction

Hydrogen is produced via serpentinization in high-temperature reactions (>200 °C), where ferrous iron (Fe^{2+}) contained in olivine and pyroxenes is converted to ferric iron (Fe^{3+}) in the secondary minerals serpentine and magnetite, liberating hydrogen (Andreani et al., 2013; Janecky & Seyfried, 1986). Low-temperature (<200 °C) serpentinization, typically occurring off-axis, also liberates hydrogen via the production of Fe-bearing brucite and serpentine (Klein et al., 2014). This process is a fundamental reaction occurring on Earth, requiring only the reaction of water with exposed ferrous iron-bearing mantle minerals. Consequently, the hydrogen produced by this reaction is considered instrumental for theories about the emergence of life in the early Earth (e.g. Canfield et al., 2006; Russell et al., 2010) and the importance that

it plays in sustaining life in the subsurface (Charlou et al., 2002; Shock & Holland, 2004) as it represents an alternative basal energy pathway from photosynthesis. Abiotic methane is also observed at ridges, though even more poorly constrained. Proposed sources include Fischer-Tropsch-type or Sabatier reactions (see review by McCollom, 2013) or degassing of deep fluid inclusions (e.g. Grozeva et al., 2020; Klein et al., 2019; McDermott et al., 2015; Wang et al., 2018). In the Phanerozoic, the most common and regular exposure of the mantle minerals to water, which lead to these reactions, occurs at mid-ocean ridges (MORs).

The upper oceanic lithosphere consists of oceanic crust overlying the mantle lithosphere. The typical, volcanic crustal profile is produced predominantly at fast-spreading (>40 mm/a) ridges, where decompression melting and the geotherm are sufficient to induce significant melting (Niu & Hékinian, 1997; Sinton & Detrick, 1992). However, at slow (20–40 mm/a) and ultraslow (<20 mm/a) ridges, the geotherm is insufficient to induce substantial melting close to the surface of the lithosphere (e.g. Turcotte & Morgan, 1992), and instead detachment faulting occurs, resulting in the asymmetric tectonic exhumation of the mantle and emplacement of deep-seated magmatic rocks into the lithospheric column (Reston & McDermott, 2011; Tucholke et al., 2008). At ultraslow ridges, these detachment faults are incredibly prominent, thought to accommodate nearly all divergence (e.g. Southwest Indian Ridge, Sauter et al., 2013), while at slow ridges they are less prevalent, accommodating up to 70% of divergence (e.g. Mid-Atlantic Ridge, Escartín et al., 2008). It is at these ridges that water principally interacts directly with a substantial volume of mantle-derived rocks producing the extensive serpentinized systems that are observed along ridge axis hydrothermal fields, such as the Lost City and Rainbow fields along the mid-Atlantic Ridge (e.g. Charlou et al., 2002; Kelley et al., 2005).

As oceanic lithosphere is continually formed at MORs, hydrogen production should be a ubiquitous process through time, controlled by the access of ocean water to ultramafic rocks (Dick, 1989). Within this ubiquitous global scale process, the primary control of serpentinization at MORs is the tectonic exhumation rate of oceanic lithosphere that modulate reaction kinetics, which are—geologically—quite a rapid process. This is because the exhumation rate is what controls fluid penetration into the upper oceanic lithosphere due to the extensive faulting of the system that occurs during exhumation, and secondly, it provides a continual source of fresh peridotite to undergo alteration (Cannat, 1993). We limit our study to the first 1 Ma of any segment of oceanic lithosphere produced at a ridge, consequently off ridge axis (i.e., ridge flank and subduction zones); serpentinization is not explicitly considered in this study. Though beyond the scope of the present contribution, the framework that our model provides (e.g., Merdith et al., 2019) could be extended to analyze ongoing serpentinization in these off-axis environments.

A limiting factor in quantifying the hydrogen flux from serpentinization processes through geological time is the incomplete geophysical and geochemical characterization of oceanic lithosphere away from the ridge axis across all ocean basins. Although laboratory experiments have measured hydrogen fluxes from serpentinization (e.g., Klein et al., 2015; McCollom et al., 2016), hydrogen has a negligible geological residence time in oceanic rock and water systems meaning the only suitable natural proxy to observe fluxes from mid-ocean ridge environments are measurements of the redox state of iron in recovered abyssal serpentinized peridotites (i.e., $FeO/(FeO + Fe_2O_3)$, Andreani et al., 2013; Klein et al., 2014). Consequently, global hydrogen and methane budgets from ridge environments are unknown through geological history. Our approach to bypass this uncertainty is to use global full-plate models (Gurnis et al., 2012) that trace the kinematic evolution of plate boundaries through time to characterize the spatial and temporal evolution of slow and ultraslow MORs (Seton et al., 2012). Quantifying the evolution of these ridges can constrain the tectonic conditions of serpentinization and thus hydrogen and methane production. Here we use the full-plate reconstruction of Matthews et al. (2016) to facilitate the analysis of ancient oceanic lithosphere and spreading ridges and calculate the primary, abiotic production of hydrogen from serpentinized mantle peridotites at ridge-axis environments for the past 200 Ma.

1.1. Present-Day Estimates

Exposure of mantle peridotites at slow and ultraslow spreading ridges has been used to create estimates at present-day of the hydrogen produced through serpentinization reactions. All studies distinguish between ultraslow–slow ridge systems and those spreading faster; however, they differ in how they quantify the effect of serpentinization and constrain the tectonic parameters. Previous studies used bulk rock properties and flat proportions of serpentinized peridotite, tied to seafloor production rates on an annual basis to

constrain the volume of hydrogen produced (see Konn et al., 2015 for a recent review), with estimates ranging from 0.8–1.3 • 10^{11} mol/a (0.16–0.26 Mt/a) (Canfield et al., 2006; Charlou et al., 2010) to 1.9 • 10^{11} mol/a (0.38 Mt/a) (Sleep & Bird, 2007). Other studies have analyzed the contribution to global hydrogen budgets specifically from iron in basalts in ocean crust (4.5 ± 3 • 10^{11} mol/a [0.9 ± 0.6 Mt/a]; Bach & Edwards, 2003) and the contribution purely from transform offset faults (6.1–10.7 • 10^{11} [1.23–2.15 Mt/a]; Rüpke & Hasenclever, 2017).

Cannat et al. (2010) estimated the depth of serpentinization using seismic data to better constrain the volume of serpentinite produced following exposure of mantle peridotite to ocean water. They calculated a hydrogen production of 0.33–4.1 • 10^{7} mol/a (6.6–82.7 t/a) per km of ridge spreading slower than 40 mm/a (roughly 15,000 km, assuming spreading asymmetry of 50%) and a mean exhumation (spreading) rate of 11.4 mm/a, to suggest that ~6.7 • 10^{11} mol/a (~1.35 Mt/a) of hydrogen is liberated at present day. Similarly, Worman et al. (2016) built upon the model of Cannat et al. (2010) by scaling hydrogen production based on the volume of serpentinized peridotite that is produced at ridges with varying spreading rate (0.5–2 km at slow and ultraslow ridges, 0.2–0.8 km at fast ridges). Their results were an order of magnitude higher than any other, suggesting that 1.2 • 10^{12} mol/a (2.4 Mt/a) of hydrogen is liberated globally ridges at present day. Finally, Rüpke and Hasenclever (2017) built a numerical model to quantify hydrogen production at oceanic-transform faults and determined that—due to increased water penetration—they can produce similar order of magnitude of hydrogen as MORs (6.1–10.7 • 10^{11} mol/a, 1.2–2.2 Mt/a). Our approach here differs from previous estimates in that we link our estimates of serpentinized lithosphere explicitly to the seafloor production rates that we determined for each ridge segment on the Earth for the past 200 Ma. This allows our methodology to accommodate temporal and spatial variations in the distribution of slow spreading ridges to determine how hydrogen production from serpentinization varies through time.

2. Present-Day Constraints

The seafloor spreading processes that we use to construct our model, such as the tectonic exhumation of peridotite and seafloor isochron preservation, typically occur on a ~1 Ma timescale. This means that our analysis can only be insightful at this length of time, at a minimum. Consequently, our model integrates processes over this timeframe, using the along ridge-axis length of a segment for these 1 Ma intervals, making it impossible for us to capture subridge segment and submillion-year trends in our approach. We can therefore estimate—on a 1 Ma timescale—the bulk properties and proportion of the expected lithologies (i.e., bulk rock volume of volcanics, peridotites, and degree of serpentinization) in our "prism" of rock defined by the half spreading rate, the depth to unserpentinized lithosphere, and the ridge segment length. But, this model cannot infer their spatial distribution or interrelationship with each other *within that prism of lithosphere*, as can be interpreted from natural observations (e.g., seafloor mapping and vertical cross-sections from drilling and dredging). Nevertheless, the "bulk" properties that we use to make this general, global model, are based on natural observations. To take into account the variability of the natural system, we consider ranges of values for the main parameters as described and inferred from dredges, drilling cores, and seismic data. The model then samples these ranges ($N = 10{,}000$) in order to produce a distribution of expected hydrogen production (Table 1). This is advantageous as it is easily and quickly updated and refined in future as more data are available and avoids us having to explicitly define a single value for any one parameter for every ridge segment through time.

To quantify hydrogen production through time, we assume a uniformitarianism evolution of Earth, whereby we extrapolate that ocean basins have been spreading under similar principles for the Mesozoic and Cenozoic. A flowchart of our methodology is presented in Figure 1, and Table 1 summarizes the distributions with some key references. Our model files are released as part of this publication in order to facilitate further work within the community and also to allow other researchers who want to test other parameter range to reassess the model with their preferred values.

2.1. Plate Boundary Reconstructions

We use the open-source *GPlates* software (Boyden et al., 2011; Müller et al., 2018) and *pyGPlates* library (www.pygplates.com) for python to access kinematic plate models that reconstruct the configuration and evolution of plates and plate boundaries over specific periods of time (see Supp. Material 2). We adopt the

Geochemistry, Geophysics, Geosystems

10.1029/2019GC008869

Table 1
Model input parameters

Spreading ridge classification	Parameter	Model inputs	Key reference(s)	Constraining data
Ultraslow spreading ridge (<20 mm/a)	Length	Within model	Matthews et al. (2016)	
	Depth to unserpentinized mantle	Data 1: 3 to 4 km; data 2: 3 to 8 km	For data 1: Minshull et al. (2006); Cannat et al. (2003); Muller et al. (1999); Michael et al. (2003); Meyzen et al. (2003). For Data 2: Chen (1992)	Seismic data
	Proportion of peridotite exhumed (i.e., divergence accommodated by tectonic accretion)	80–100%	Sauter et al. (2013); Tucholke et al. (2008)	Dredge; seafloor morphology; numerical modeling
	Degree of serpentinization	80–100%	Cannat et al. (2010)	Seismic data; IODP cores
Slow spreading ridge (20–40 mm/a)	Length	Within model	Matthews et al. (2016)	
	Depth to unserpentinized mantle	3–4 km for amagmatic segments, up to 7 km if magmatic	Bown and White (1994)	Seismic data
	Proportion of peridotite exhumed	12.5–80%; average 50%	Carlson (2001); Tucholke et al. (2008)	Dredge; seafloor morphology; numerical modeling
	Degree of serpentinization	20–100%		Seismic data; IODP cores
Intermediate spreading ridge (40–70 mm/a)	Length	Within model	Matthews et al. (2016)	
	Depth to unserpentinized mantle	7 ± 1 km	Bown and White (1994)	Seismic data
	Proportion of peridotite	5–15%	Constantin et al. (1995)	Dredge (adjacent to transform fault)
	Degree of serpentinization	0–20%	Constantin et al. (1995)	Dredge (adjacent to transform fault)
Fast spreading ridge (70–180 mm/a)	Length	Within model	Matthews et al. (2016)	
	Depth to unserpentinized mantle	7 ± 1 km	Bown and White (1994)	Seismic data
	Proportion of peridotite	0–10%	Constantin et al. (1995)	Dredge (adjacent to transform fault)
	Degree of serpentinization	0–10%	Constantin et al. (1995)	Dredge (adjacent to transform fault)
Transform segments	Length	Within model	Matthews et al. (2016)	
	Depth to unserpentinized mantle	7 ± 1 km	Global average	
	Proportion of peridotite	0–100%	Dick (1989)	Dredge
	Slip rate	Within model		
	Degree of serpentinization	20–80%	Dick (1989)	Dredge

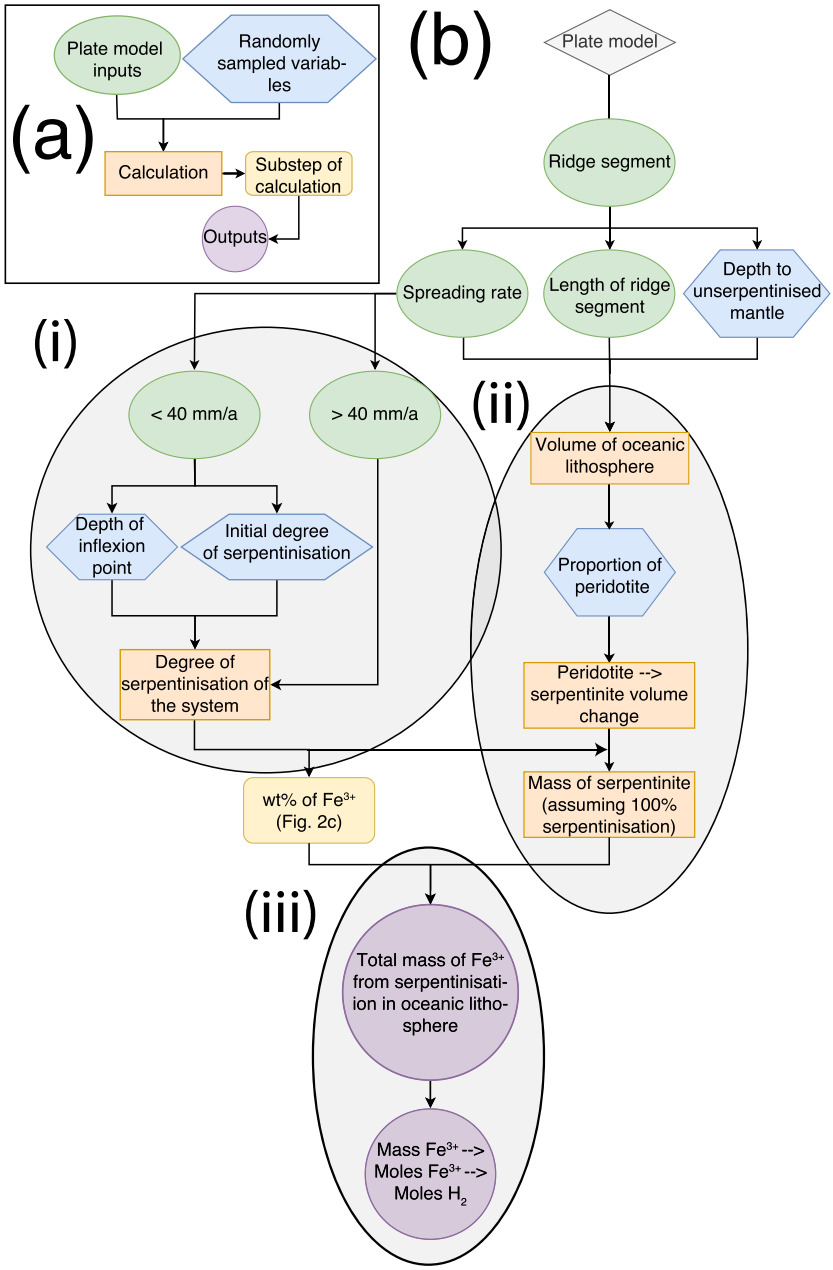

Figure 1. Flow chart describing our methodology. (a) Summary and breakdown of color-coded steps: green, plate model inputs; blue, tectonic variables determined from present-day data; orange and yellow, calculation steps; purple, outputs (moles of H_2, mass of serpentinite. etc.). (b) Detailed flowchart showing the inputs, outputs, and dependencies of each variable broken into three separate stages. Calculate (i) the degree of serpentinization of the system; (ii) total mass of serpentinite formed; and (iii) volume of hydrogen produced (see Section 2.5).

model of Matthews et al. (2016) for the period comprising the Jurassic to present day (200 to 0 Ma), which is a compilation of the Müller et al. (2016) model for 230 to 0 Ma and the Domeier and Torsvik (2014) model from 410 to 250 Ma. The model includes the corrections outlined by Torsvik et al. (2019). We focus our model for hydrogen production and discussion on the 200 to 0 Ma period because the kinematic plate motion reconstruction models are better constrained within this period. This is to minimize the uncertainties inherent to plate reconstructions by avoiding using "synthetic mid-ocean ridge segments," which must be utilized to construct full-plate models prior to Pangea where there is no preserved in situ oceanic lithosphere.

We use the topological plate boundary network of Matthews et al. (2016) to extract the lengths of spreading plate boundaries at 1 Ma time increments. This computation yields the total cumulative length of the MOR system, which includes both the transform and spreading segments. We separate these segments from each other by filtering based on a deviation angle (70°) between the alignment of the segment to the stage pole that defines the rotation. Spreading rates of each spreading segment and slip rates of each transform segment. We include the lengths and slip rates of oceanic transform faults (OTFs), in addition to transform segments at MORs, for the last 200 Ma as they are also known to expose sections of serpentinite and mantle peridotite (Constantin et al., 1995; Dick, 1989; Fox et al., 1976) and are thought to provide a significant component to the serpentinized-liberated hydrogen budget (e.g., Rüpke & Hasenclever, 2017). Relict strike-slip plate boundaries, evidenced by fracture zones, are defined by valleys 1 to 6 km deep and 15 to 40 km wide (Dick, 1989), and changes in the azimuth and velocity of plate motion over time can cause broad heterogeneities that are impossible to capture through dredged material (Fox et al., 1976). For this analysis we use a fixed width of 1 km for each OTF segment; however, more meaningful incorporation of OTFs and fracture zones (MacLeod et al., 2017; Matthews et al., 2011) into the hydrogen budget should be an important and interesting developmental avenue.

2.2. Spreading Rates and Spreading Asymmetry

We classify spreading ridges into four categories based on their full spreading rate: ultraslow (0–20 mm/a), slow (20–40 mm/a), intermediate (40–70 mm/a), and fast (>70 mm/a), with the most important distinction between slow and intermediate ridges (here at 40 mm/a) after Cannat et al. (2010) and Worman et al. (2016). The transition at 40 mm/a is important because this is the spreading rate above which MOR systems begin to transition between the cooler, amagmatic ridges dominated by tectonic accretion to warmer spreading regimes controlled by magmatic accretion (e.g., Canales et al., 2005; Dick et al., 2003; Small, 1994). This is supported by numerical modeling, which indicates that as spreading rates approach 40 mm/a, the thickness of oceanic crust is stabilized at 6–8 km (Crameri et al., 2019). Dick et al. (2003) place the transition between slow and intermediate slightly higher, at 55 mm/a, we opt for a more conservative value for two reasons. Firstly, the transition between tectonic and magmatic accretion begins at 40 mm/a (Dick et al., 2003) meaning that while spreading rates faster than 40 mm/a may result in tectonic exhumation of the mantle, it will be governed by factors more complex than spreading rate, which cannot be determined through time and are beyond the scope of this work. Secondly, the stability of serpentinite is limited at ridges spreading faster than 40 mm/a because the thermal gradient is too high (e.g., Rüpke & Hasenclever, 2017).

For our analysis we define spreading asymmetry as the distinct proportion of differing volumes of oceanic crust formed and preserved on each ridge flank integrated on a 1 Ma timescale. It occurs variably at all ridges, though appears more prominent at slow and ultraslow ridges (e.g., Crameri et al., 2019; Müller et al., 2008). At ridges spreading below 40 mm/a, asymmetry is as high as 60%, along segments of the Southwest Indian Ridge and Northern Mid-Atlantic, though these appear to be outliers, with the cluster of data for slow and ultraslow ridge segments showing a mean that is much lower, between 10 and 20% asymmetry (Crameri et al., 2019). In effect the increasing asymmetry with decreasing spreading rate is a function of the increasing proportion of tectonic accretion, at the cost of magmatic accretion, that occurs at ultraslow and slow spreading segments (e.g., Tucholke et al., 2008). Here, as asymmetry increases (i.e., as magmatism decreases), spreading is isolated predominantly on a single ridge flank, with some remnant magmatism being erupted onto the adjacent flank (Tucholke et al., 2008). Our approach accommodates spreading asymmetry because we use the full spreading rate (i.e., both flanks summed) to determine the mode of spreading (magmatic vs. amagmatic) and the volume of rock generated.

2.3. Thickness of Upper Oceanic Lithosphere and Distribution of Ultramafic Rocks

The thickness of the upper oceanic lithosphere (defined here as the depth to unserpentinized mantle) and the production and distribution of ultramafic rocks along ocean ridges are first-order controls on the available mass of rocks for serpentinization reactions. Intermediate and fast spreading rates produce a “normal” layered oceanic crust, ~6–8 km thick, consisting of pillow basalts, dykes, gabbros, and peridotites (e.g., Alt & Teagle, 1999). Comparably, crust at slow and ultraslow ridges is thinner, where not absent, driven by a cooler isotherm that inhibits extensive melt generation and migration (e.g., Turcotte & Morgan, 1992). Minshull et al. (2006) describe the depth to unserpentinized mantle for ultraslow ridges ranging from 3 to 4 km, and Cannat et al. (2003) describe the depth as ranging from 3 to 8 km but typically between 2 to 4 km.

Seismic data suggest that heterogeneous lithosphere exists to a depth of 3 to 4 km beneath ridges spreading slower than 40 mm/a (Canales et al., 2000; Cannat et al., 2010); however, some recent studies suggest that localized serpentinization can extend to great depths (~10 km) along detachment faults accommodating plate divergence (e.g., Cannat et al., 2019). This could lead to an increased estimate of hydrogen flux, dependent on the degree of rollback of the detachment fault.

The proportion of peridotite exposed along ridges is largely unknown, and variations in the density of sampling at spreading ridges render a robust statistical treatment for distribution along MORs difficult (Baker & German, 2004). At ridges spreading below 40 mm/a, mantle peridotite is exposed mostly along detachment faults by unroofing of the mantle and in extensive megamullion complexes (Alt et al., 2013; Cannat, Mevel, et al., 1995, 2010; Dick et al., 2008; Reston & McDermott, 2011; Tucholke et al., 1998, 2008; Tucholke & Lin, 1994). Asymmetric spreading at ultraslow and slow ridges occurs because the tectonic exhumation of the mantle occurs only on one flank at a time, with some volcanics being emplaced in the hanging wall (e.g., Escartín et al., 2003) and some magmatic bodies emplaced at depth within peridotites in the footwall. As the spreading system evolves, the exhumation can flip to the opposite flank, providing new crust on both margins over million-year timescales.

The proportion of ultramafic rocks at ultraslow ridges is estimated to be as high as between 80 and 100% (Sauter et al., 2013), with slower ridges exhibiting much greater variability. A distinguishing morphological feature between these two spreading ridges is seafloor smoothness, with continual faulting (such as at the SWIR) producing smooth seafloor, while periodic volcanism (as is more common at slow ridges) offsets the faults, creating corrugated seafloor (Cannat et al., 2006). Tucholke et al. (2008) showed—through numerical modeling—that at slow spreading ridges detachment faulting occurs when between ~30 and 50% of divergence is accommodated by magmatism (i.e., the remainder 50 to ~70% of divergence occurs through detachment faults). When magmatism is less than 20%, the resulting divergence is accommodated almost entirely by faulting, such as at the Southwest Indian Ridge (SWIR) (Cannat et al., 2006). We therefore put 80% of seafloor divergence accommodated by detachment faulting (i.e., 80% of "crust" is exhumed peridotite) as our break between slow and ultraslow ridges (Table 1). At intermediate and fast spreading ridges, peridotite also occurs in a local scale along fractures zones (Constantin et al., 1995; Früh-Green et al., 1996, 2001; Hekinian et al., 1996; Niu & Hékinian, 1997) such as those of the ultrafast East Pacific Rise (Anderson & Nishimori, 1979; Hébert et al., 1983) and at the bottom of the oceanic crust as part of the uppermost mantle lithosphere. Two cores have drilled through intermediate (Deep Sea Drilling Project [DSDP] hole 504B; ~1,500 m, deep at the Costa Rica Rift, Becker et al., 1989) and fast (International Ocean Drilling Program [IODP] hole 1256D; ~1500 m deep at the East Pacific Rise, Wilson et al., 2006) ridges, in both cases no peridotite (or serpentinized peridotite) was recovered. However, Carlson (2001) suggested that up to 5% of the lower oceanic crust could be serpentinized as it cannot be resolved from seismic data. As we cannot discount that some serpentinization of peridotite occurs at intermediate and fast ridges, either at the base of the crust, or in proximity to transform faults, we infer a very small proportion of peridotite available for serpentinization at these ridges (<15%).

2.4. Degree of Serpentinization and Mass of Ferric Iron

The degree of serpentinization is extremely important for determining how much ferric iron is produced, as the behavior of the serpentinization reaction varies depending on the degree of progression of the system (Andreani et al., 2013). Ferrous iron in peridotite is converted into ferric iron and stored in magnetite and serpentine, liberating in the process elemental hydrogen (in this study we only consider magnetite and serpentine, though other minerals, such as andradite or chlorite, can also store ferric iron). At lower degrees of serpentinization, ferric iron is more readily taken into serpentine, while at higher degrees, it is also incorporated in magnetite. Consequently, even at lower degrees of serpentinization, a substantial amount of ferric iron, and consequently, hydrogen, can be produced (e.g., Andreani et al., 2013; Klein et al., 2014). Unfortunately, the degree of serpentinization is perhaps the most difficult parameter to determine, as it has a broad spatial, temporal, and depth variability (e.g., Cannat et al., 2010). This is because seismic velocities of partially serpentinized peridotites (20–50% serpentinized) are indistinguishable from gabbro (Carlson, 2001; Miller & Christensen, 1997), meaning there is no large-scale method available to approximating either the degree or volume of serpentinization in oceanic crust at depth.

Furthermore, the majority of reports on serpentinization degree usually state whether the peridotites are fresh (none–little serpentinization) or have suffered serpentinization to an unknown (usually assessed qualitatively) degree.

As a general constraint, peridotites in ridges spreading slower than 40 mm/a exhibit highly variable degrees of serpentinization ranging from 20 to 100% (Bonnemains et al., 2016; Klein et al., 2014, 2017; Toft et al., 1990). At these ridges the degree of serpentinization has a depth dependency relative to the degree of fluid penetration (Cannat et al., 2010). IODP hole 1309D, which cored 1400 m through gabbro in the Atlantis Massif (e.g., Ildefonse et al., 2007), showed alteration degrees of 30–80% to a depth of 800 m, before tapering down to less than 20% (Delacour et al., 2008). No similar core exists for exhumed peridotite with which we can use as a direct constraint. IODP holes 920B and 920D cored serpentinites in another location along the mid-Atlantic ridge (MARK area), however only to a depth of 120 m (Karson et al., 1997). These cores dominantly consisted of serpentinized peridotite, typically ranging between 80 and 100% serpentinized but locally as low as 20% depending on parent lithology (Cannat, Karson, et al., 1995). To supplement IODP core data to constrain the bulk degree of serpentinization, we also consider seismic data. Though seismic surveys are subject to high degrees of uncertainty, density variations of upper oceanic lithosphere at the mid-Atlantic ridge exist and have been mapped (e.g., Canales et al., 2000; Dannowski et al., 2010). These studies support an interpretation that emplaced peridotites are serpentinized between 80 and 100% to a depth of 800 to 1200 m, before tapering linearly to 0% serpentinization at a depth between 3200 and 4000 m (Figure 2(a), Oufi et al., 2002; Cannat et al., 2010). We therefore consider a shallowest limit of 800 m for extensive fluid penetration (e.g., IODP hole 1309D) and 1200 m as the deepest level. Both seismic data and core data show that alteration does not trend to 0 immediately after this limit but instead can be maintained at a low degree for the middle–lower crust. We therefore adopt the parameterization of this data constraining degree of serpentinization after Merdith et al. (2019). As for the proportion of peridotite at intermediate and fast ridges described earlier, we cannot rule out that some serpentinization does occur at these ridges; hence, our model includes very low degrees of serpentinization (<15%) of peridotite at these ridges.

Our model incorporates and captures the relationship between the degree of serpentinization and the corresponding wt % of ferric iron produced from serpentinization reactions of abyssal peridotite (e.g., Andreani et al., 2013; Klein et al., 2014, Figure 2(c), Supp. Material 1). The redox data compilation excludes data from serpentinites collected from other tectonic settings such as ophiolites or subduction zones. This results in a much smaller sample space as compared to the compilation of Evans (2008), with degrees of serpentinization ranging from 20–100% and ferric iron from 1–7 wt% (Figure 2(c)). The resulting overall degree of serpentinization of our system (i.e., Figure 2(a)) is used to then isolate a distribution of possible ferric iron wt% (i.e., a vertical line drawn through Figure 2(c)), truncated by the uncertainty [gray] bands in the data). We randomly select a value from that distribution, which becomes the ferric iron wt% that we pass into our calculation.

2.5. Calculating Hydrogen Flux

Our model comprises three main components (Figure 1), defined by the calculation of (i) the degree of serpentinization of the system; (ii) the volume of serpentinites; and (iii) the potential amount of ferric iron and hydrogen produced. In the construction of this model we tested both normal and uniform distribution of the range of parameters listed in Table 1. The difference applying either distribution is negligible. For clarity, results are presented using uniform distributions, but the code that is provided with this publication has an option to sample the variables from a truncated normal distribution if desired.

1. The volume of reactants (i.e., mantle peridotite) that can undergo serpentinization to produce hydrogen at MORs is calculated by multiplying the spreading rate (km/Ma), the depth to unserpentinized lithosphere (km) and ridge length (km) of an individual ridge segment at each time interval (1 Ma). This is then multiplied by the proportion of peridotite to obtain the total volume of peridotite available for serpentinization in kg/km^3. The volume change for serpentinization of peridotite for a Fe-conservative system is accounted for using data in Andreani et al. (2013). This yields a (theoretical) maximum volume of serpentinite generated from which we apply redox geochemical pathways (steps ii and iii) to evaluate ferric iron, hydrogen, and methane production at 1 Ma intervals for the past 200 Ma.

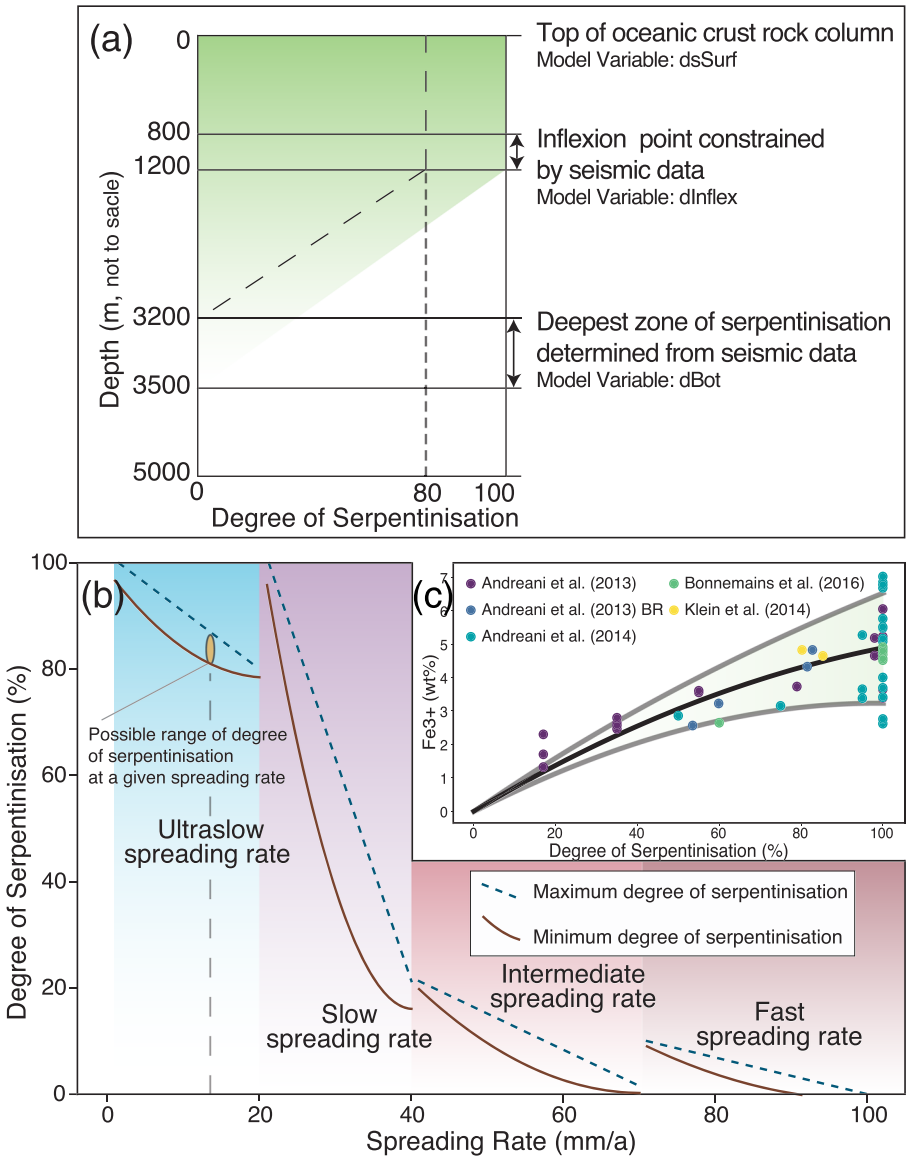

Figure 2. (a) Relationship between depth and degree of serpentinization (for ultraslow and slow ridges only), ds_{surf}, d_{inflex}, and d_{bot} refer to degree of serpentinization at surface, depth to the inflection point (when serpentinization starts to decrease linearly with depth), and depth to bottom of serpentinization, respectively. Depth values are taken from Cannat et al. (2010) and are based on seismic profiles revealing the depth and degree of serpentinization. The shaded blue area is summed and becomes our degree of serpentinization for each ridge segment. (b) Spreading rate and degree of serpentinization that are used to determine ds_{surf} in our calculations for ultraslow and slow ridges or the average degree of serpentinization at intermediate and fast ridges (since mantle peridotites are not exhumed at these ridge types); for each ridge classification (ultraslow, slow, etc.) we create an inverse relationship (blue dotted lines) between spreading rate and degree of serpentinization to act as an upper limit on the maximum possible degree of serpentinization, either at the top of the lithospheric column (in the case of slow and ultraslow ridges) or as an average throughout the column (for intermediate and fast). We introduce some variance into the model by constructing a second curve that describes the minimum degree of serpentinization (red solid lines) such that our methodology samples the resulting parameter space. We ensure that the minimum degree of serpentinization is also within the prescribed ds_{surf} bounds established from the literature. The minimum degree of serpentinization tapers at the limit of each spreading system classification (e.g., 100% and 80% for ultraslow and 80 and 20% for slow), in order to address some uncertainty in spreading rate histories of the ocean plates (i.e., a plate spreading at 19 mm/a with 10–15% uncertainty [e.g., Müller et al., 2008] might actually have been spreading at 21 mm/a, by tapering the ends we try to ensure that adjacent spreading rates result in nearly adjacent ds_{surf} values). A truncated uniform distribution of the values between the two lines (e.g., orange ellipse in (b)) is calculated per spreading rate of each ridge segment, at each time step, and a degree of serpentinization is selected at random from this range. (c) Distribution of the degree of serpentinization and wt % of ferric iron, see Supp. Material 1 for the table. Black line is mean, with gray lines one standard deviation. Data were taken from Andreani et al. (2013); Andreani et al. (2014); Bonnemains et al. (2016); and Klein et al. (2014).

2. For slow and ultraslow ridges, we calculate the degree of serpentinization (DS) by determining the area as a percent of total of the lithospheric profile in order to capture the variation of serpentinization degree with depth (Figure 2(a), Equation 1).

$$DS = \frac{DS_{surf} \bullet d_{infelx} + \left(\frac{\left(d_{bot} - d_{infelx}\right) \times DS_{surf}}{2} \right)}{d_{bot}} \bullet 100, \quad (1)$$

with DS_{surf} being the degree of serpentinization at the surface of the oceanic lithosphere; d_{infelx} the depth of the inflection point; d_{bot} the depth of unserpentinised mantle (e.g., Figure 2(a)). We initialize the calculation by determining DS_{surf} by randomly selecting a value from a uniform distribution (Figures 1(b) and (c)) defined by the difference between an inverse linear relationship with spreading rate (dashed blue lines in Figure 2(b)) and a parabolic equation between the spreading rate cutoffs of each ridge classification (solid red line in Figure 2(b)). This approach ensures that DS_{surf} decreases as spreading rate increases. We fix any spreading rate over 100 mm/a to 100 mm/a in order to simplify this part of the calculation (for the actual crustal production rate we use the spreading rate as extracted from the plate model). A uniform distribution is constructed for the valid ranges of d_{inflex} (between 800 and 1,200 m) and d_{bot} (3,200 to 4,000 m) and a value randomly selected within each range from each parameter. This procedure allows our calculations to be consistent with lithospheric depths of serpentinization as suggested by seismic data (Cannat et al., 2010; Muller et al., 1999), while maintaining the integrity of the inverse relationship between serpentinization degree and spreading rate. As such, ridges that spread more slowly will tend to have a higher degree of serpentinization.

3. Volume of iron and hydrogen. Assuming that all iron produced from serpentinization goes into either magnetite or serpentinite, the relationship between degree of serpentinization and wt % of ferric iron in Figure 2(c) allows us to convert a volume of serpentinite into the mass of ferric iron at different degrees of serpentinization. The total wt% of ferric iron is directly proportional to the calculated volume of hydrogen generated at a single MOR or transform segment.

3. Results

3.1. Model Uncertainty

Our approach parametrizes the various tectonic facets of a MOR system to address uncertainty through statistical sampling (Figure 3). Figure 3 shows the full distribution of each parameter and illustrates the probability of encountering given conditions at a specific spreading rate. The progression of ferric iron wt% from serpentinization degree is continuous, with the slowest spreading rates (1–2 mm/a) resulting in the highest degrees of serpentinization (60–70%) and a ferric iron content of 2.5–5 wt%. These extremely low rates of spreading have not been encountered in present-day natural systems and represent the end member of ferric iron formation and hydrogen production given the lowest possible rates of spreading. At present day, the slowest spreading MOR, the Gakkel Ridge (Arctic Ocean), has a divergence rate of between ~7 and 12 mm/a (Cochran et al., 2003), which in our model suggests a degree of serpentinization of 55–65% and ferric iron content of 2–4.5 wt% (Figure 3(a)). Comparably, the Indian Ocean between 80 and 50 Ma, which has a divergent rate in excess of 80 mm/a, has an extremely low degree of serpentinization and corresponding ferric iron content (0–10% and 0–0.8 wt%, respectively). Other ocean basins are plotted for reference in Figure 3(a). The correlation between all variables is also expressed in the covariance matrix (Pearson correlation coefficient, Figure 3(b)), with the probability distribution for individual variables as a function of spreading rate of the system highlighted in subsequent panels (Figures 3(c)–(f)). The distributions of serpentinization degree and proportion of peridotite exhumed (Figure 3(c)) are more discrete, with breaks at spreading rates of 20, 40, and 70 mm/a, corresponding to the transition of different spreading regimes used in our model. The most significant transition occurs at 40 mm/a, when the model separates spreading ridges dominated by tectonic accretion with those dominated by magmatic accretion. At this transition, small changes in spreading rates will have the greatest impact on the amount of hydrogen liberated, with the influence of perturbations decreasing away from this transition. These breakpoints are also exhibited strongly in Figures 3(d) and (e), which show the distribution of proportion of peridotite and thickness, respectively. Slow ridges exhibit the greatest variability in their proportion of peridotite based on the dredge record and seismic data, which suggest either low or high volumes of mantle exhumation (e.g., Carlson, 2001).

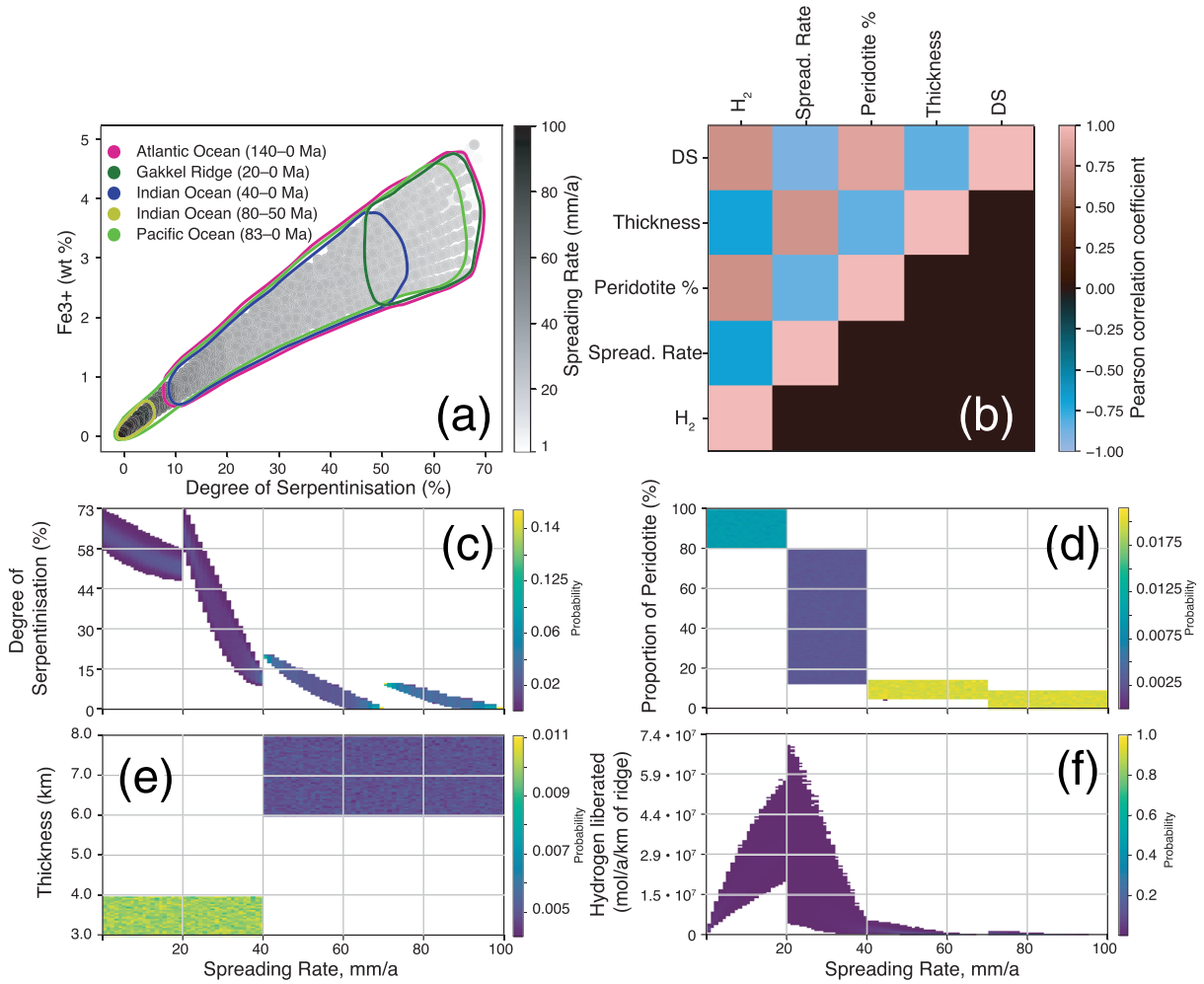

Figure 3. Summary of uncertainty and variable range from our analysis. Each sample space was determined using 10,000 iterations. (a) Sample space of ferric iron wt% given a total degree of serpentinization of the crustal unit (spreading-rate • thickness • segment length), colored by spreading rate. The colored polygons represent spreading systems extracted from the Matthews et al. (2016) plate model and were constructed by filtering the data using the mean and one standard deviation spreading rate of the respective spreading systems. Atlantic Ocean, 140–0 Ma, 27 ± 13 mm/a; Gakkel ridge, 20–0 Ma, 12 ± 6 mm/a; Indian Ocean, 40–0 Ma, 32 ± 7 mm/a; Indian Ocean, 65–50 Ma, 12 ± 5 mm/a; Pacific Ocean, 83–0 Ma, 71 ± 57 mm/a. (b) Pearson's correlation matrix showing the relationship of each parameter used in the analysis. (c–f) Distributions of parameters at each spreading rate from 1–100 mm/a per 1 km of ridge length. (c) Degree of serpentinization, (d) proportion of peridotite exhumed, (e) thickness, and (f) moles of hydrogen liberated. These panels are to be read as a vertical histogram at each point along the *x*-axis, given the expected distribution of the parameter at each spreading rate. Therefore, the lower and upper bounds of each distribution are defined by the minimum and maximum constraints outlined in Table 1, respectively. For example, the lower bound between 0 and 20 mm/a in panel (f) is defined by a proportion of peridotite of 80%, ds_{surf} of 80%, d_{inflex} of 800 m, d_{bot} of 3,000 m and the lower intercept between overall degree of serpentinization and ferric iron content in panel (a).

Figure 3(f) is the product of the prior three panels and shows the volume of hydrogen liberated in mol/a/km of ridge. In our model spreading rates between 10 and 30 mm/a are the greatest contributors to the hydrogen budget, with intermediate and fast ridges producing an order of magnitude less hydrogen per km of ridge.

3.2. Serpentinization and Hydrogen Production Since 200 ma

Hydrogen production related to serpentinization reactions at MORs exhibits broad spatial and temporal variability between 200 and 0 Ma (Figure 4, Supp. Material 3). At present day, the most productive ridges are the Gakkel Ridge, segments of the Central and Southern Atlantic, the Southwest Indian Ridge, and the Red Sea, which individually generate more than $4 \cdot 10^{15}$ mol/Ma ($8.06 \cdot 10^{3}$ Mt/Ma) of H_2 each. Comparably, the Pacific and the Southern Ocean are relatively infertile, with H_2 production an order of magnitude lower ($0.1–1 \cdot 10^{15}$ mol/Ma, $0.2–2 \cdot 10^{3}$ Mt/Ma) (Figure 4(a)). The North Atlantic is more productive

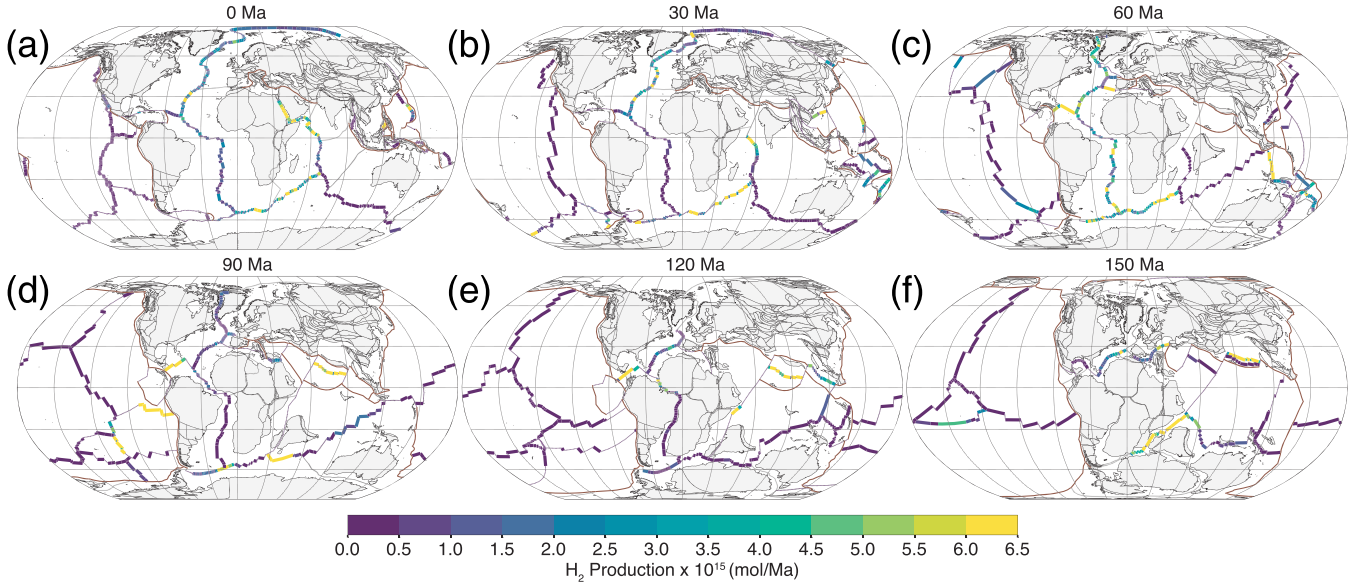

Figure 4. Spatial distribution of hydrogen productive ridges since 150 Ma using mean calculated values from 10,000 model runs (see Supp. Material 3 for an animation from 200 Ma). (a) 0 Ma; (b) 30 Ma; (c) 60 Ma; (d) 90 Ma; (e) 120 Ma; and (f) 150 Ma. Brown lines are subduction zones.

at approximately 30 Ma than present day (Figures 4(a) and (b)), with preserved spreading rates during this time consistently between 10 and 30 mm/a (Müller et al., 2008). The most hydrogen fertile ridges over the last 200 Ma occur from the Late Cretaceous to the Eocene (Figures 4(b) and (c)), with high productivity being focused through the entire Atlantic Ocean and Labrador Sea, as well as large segments of ridges in the Pacific Ocean. Hydrogen production in the Southwest Indian Ridge, including its incision into the Red Sea, is enhanced post 40 Ma, after Greater India collided with Eurasia, and spreading rates decreased from 140 mm/a to 10–50 mm/a (Figure 4(b)). However, prior to 40 Ma, our model suggests limited hydrogen production ($<1 \cdot 10^{15}$ mol/Ma, $<2 \cdot 10^{3}$ Mt/Ma) in the Indian Ocean (Figures 4(c)–(f)). In contrast, the Southeast Indian Ridge, with spreading rates in excess of 40 mm/a, exhibits relatively reduced hydrogen production throughout the entire Cenozoic and Mesozoic.

Our model also captures the tectonic evolution and potential hydrogen fertility of two major ocean basins that have experienced continual or complete subduction of their oceanic lithosphere: the Pacific and Neo-Tethys oceans. Throughout the Cenozoic and Mesozoic, now extinct or subducted ridges that evolved in the Pacific Ocean were spreading at rates greater than 40 mm/a, generating relatively reduced amounts of hydrogen. In contrast, the opening of the Neo-Tethys resulted in a hydrogen productive ($>4 \cdot 10^{15}$ mol/Ma, $>8.06 \cdot 10^{3}$ Mt/Ma) spreading ridge between 155 and 145 Ma that progressively became less fertile from 140 to 120 Ma ($<2 \cdot 10^{15}$ mol/Ma, $<4.03 \cdot 10^{3}$ Mt/Ma; Figures 4(e) and (f)).

Intense pulses of relatively high hydrogen production are correlative with the potential availability of fresh peridotite preferentially exhumed in the slow or ultraslow MORs during the kinematic evolution of the Pangea breakup. The evolving tectonic configuration from 200 to 0 Ma is shown in Figure 5(a) in terms of the change in cumulative lengths of MORs and OTFs. Changes in the global tectonic regime are reflected in the creation and growth of MORs and OTFs that control peridotite exhumation and ultimately modulate pulses of hydrogen production derived from peridotite serpentinization. Variations in MORs and OTFs configurations provide the basis for estimating the global production of hydrogen from serpentinization reactions during the Pangea breakup (Figure 5(b)). The corresponding global hydrogen production derived from serpentinization at mid-ocean ridge settings fluctuates between 0.25 and $8.0 \cdot 10^{17}$ mol/Ma ($0.05–1.6 \cdot 10^{6}$ Mt/Ma) for the past 200 Ma (Figure 5(b)), with the last 1 Ma providing a global flux of ~7–8 $\cdot 10^{17}$ mol/Ma ($1.4–1.6 \cdot 10^{6}$ Mt/Ma). This estimate does not include off-axis environments, ophiolites, continental rift settings, or passive margins. Notably, the opening of the Central Atlantic between 180 and 165 Ma signaled the appearance of the first significant slow spreading ridge and hydrogen pulse in the past 200 Ma.

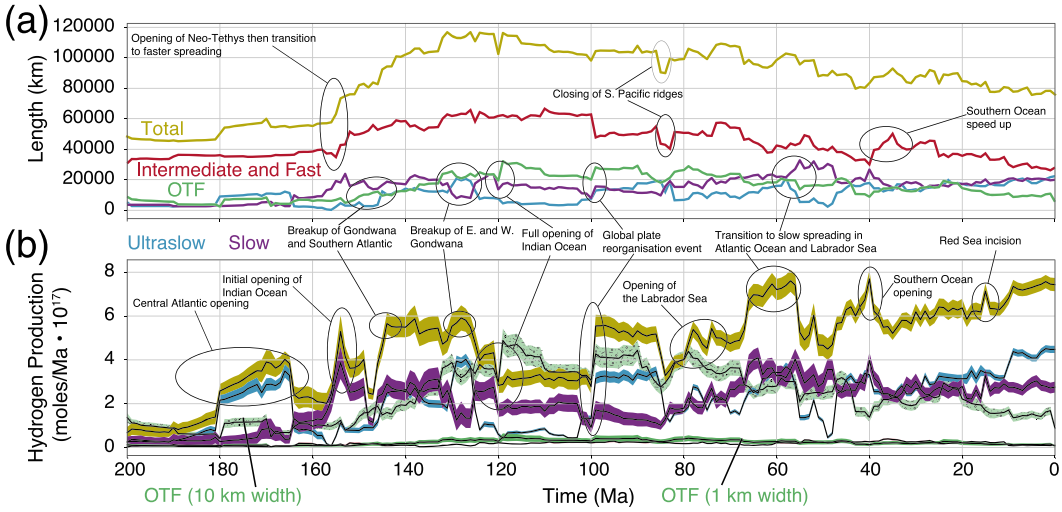

Figure 5. (a) Length of MORs and OTFs (OTFs include transform faults offsetting ridge segments and also connecting other plate boundaries through oceanic lithosphere) and (b) corresponding mean hydrogen production and two standard deviations through time after 10,000 model runs. Plate boundaries and their corresponding hydrogen production are split into intermediate and fast (spreading rate greater than 40 mm/a, red line), slow (21–40 mm/a, purple line), ultraslow (0–20 mm/a, blue line) and OTFs (green line). The gold line is the sum of all. In (b) the hydrogen production of OTFs assumes a lateral width of 1 km, which we picked conservatively, and suggests lower production of hydrogen than the modeling of Rüpke and Hasenclever (2017). However, a width of 10 km would produce values more consistent but still lower than the results of Rüpke and Hasenclever (2017). The total length in (b) uses the OTF width of 1 km *and not 10 km*. Slow and ultralow ridges both have similar lengths throughout the last 200 Ma; however, ultraslow ridges tend to contribute more hydrogen under our model.

Additionally, high pulses of hydrogen generation appear concomitantly with the initial opening of the Indian Ocean (~150 Ma) and the continual opening of the Atlantic Ocean. The partitioning of Gondwana at 140 Ma also resulted in the production of a large amount of hydrogen, with an increase from 0.75 • 10^{17} mol/Ma to 6.0 • 10^{17} mol/Ma (0.15• 10^{6} Mt/Ma to 1.2 • 10^{6} Mt/Ma) being generated and sustained for ~20–25 Ma. The opening of the Labrador Sea and transition to slow spreading for large extents of Atlantic Ocean in the Late Cretaceous and Early Paleogene drove a large pulse of hydrogen production, culminating at 56 Ma with a volume of ~7–8 • 10^{17} mol/Ma (1.4–1.6 • 10^{6} Mt/Ma). Post 40 Ma hydrogen production is relatively stable through to present day, increasing from 6 to 8 • 10^{17} mol/Ma (1.2–1.6 • 10^{6} Mt/Ma). A full table of results is provided in Supp. Material 4.

4. Discussion

4.1. Comparison to Previous Studies

Our analysis, using spreading rates derived from a full-plate motion model coupled with a parameterized model of serpentinization degree results in a present-day hydrogen flux of ~8 • 10^{11} mol/a (1.6 Mt/a) (Figures 5(b) and 6(a)) at mid-ocean ridges. Most previous estimates of hydrogen production from serpentinization suggest fluxes ranging 0.8–2 • 10^{11} mol/a (0.16–.40 Mt/a) of hydrogen at present-day MORs using both a fixed spreading rate (i.e., a fixed volume of new crust formed around the globe equally divided amongst all ridges) and bulk degree of serpentinization (Canfield et al., 2006; Kasting & Canfield, 2012; Sleep & Bird, 2007). More recent studies have explored the effects of varying either the degree of serpentinization (Cannat et al., 2010), resulting in a flux estimate of 0.48–6.01 • 10^{11} mol/a (0.1–1.2 Mt/a), or both spreading rate and the degree of serpentinization (Worman et al., 2016), resulting in an even higher estimate of ~1.2 • 10^{12} mol/a (2.42 Mt/a) (Figure 6(b)). Our estimates oscillate between those of Worman et al. (2016) and Cannat et al. (2010). Outside of ridge environments, other sources of hydrogen derived from serpentinization include active subduction zones (e.g., Vitale-Brovarone et al., 2017) and continental rifting that leads to hyperextended passive margins (e.g., Manatschal et al., 2015). Our analysis does not yet include either of these environments. However, the model presented here could be extended "forwards" in time to subduction

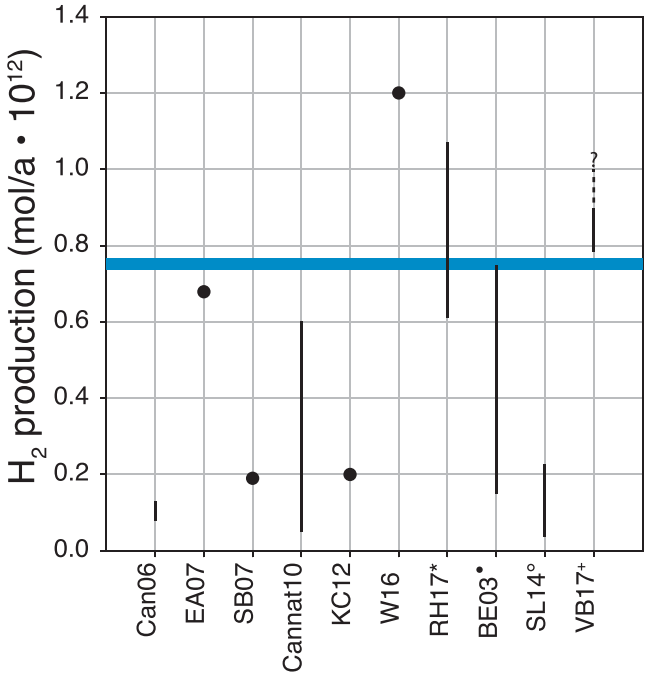

Figure 6. Estimates from previous studies of hydrogen production in various tectonic settings at present day. Blue horizontal line is our result. From serpentinized lithosphere at mid-ocean ridges: Can06, Canfield et al. (2006); EA07, Emmanuel and Ague (2007); SB07, Sleep and Bird (2007); Cannat10, Cannat et al. (2010); KC12, Kasting and Canfield (2012); W16, Worman et al. (2016). *From oceanic transform faults: RH17, Rüpke and Hasenclever (2017). •From olivine in basaltic crust: BE03, Bach and Edwards (2003). °From Precambrian continental crust: SL14, Sherwood Lollar et al. (2014). +From serpentinization in subduction zones (no upper limit was given): Vitale-Brovarone et al. (2017).

zone settings (e.g., Merdith et al., 2019) or "backwards" in time to continental rifting, but this is beyond the scope of the present contribution.

The key reason for our increased estimates relative to earlier estimates in ocean basins is because our study (and that of Worman et al. (2016)) treats both the degree or serpentinization and proportion of peridotite as a free parameter at any given ridge segment. We agree with Worman et al. (2016) that slow and fast ridges need to be treated differently; however, we extend this even further by grading our estimates to the preserved spreading history of each unique mid-ocean ridge segment, as there is a further dichotomy between the proportion of peridotite and degree of serpentinization at slow and ultraslow ridges (Table 1, Dick et al., 2003; Tucholke et al., 2008). We note however that our analysis specifically does not include serpentinization of olivine in basalts or pyroxenes in gabbros (e.g., Bach & Edwards, 2003), which will constitute an additional contribution to hydrogen production from altered oceanic crust in ridge environments.

Worman et al. (2016) assumed a fixed amount of hydrogen liberated per unit volume of serpentinized peridotite (S-P), where the volume of S-P is dependent on spreading rate, using two classes for slow (<40 mm/a, fixed value of 24 mm/a) and faster (>40 mm/a, fixed value 76 mm/a) spreading. Their results suggest that both fast and slow spreading ridges produce similar levels of hydrogen, as the spreading rate from a faster ridge offsets the higher volume of serpentinite produced at slower ridges. While we also differentiate using spreading rate, our model differs in that we scale the volume of serpentinized peridotite more strongly against spreading rate than Worman et al. (2016) (e.g., Figure 3). The consequence of this is that our parameter range for S-P (i.e., the volume of peridotite that is serpentinized) is much smaller than Worman et al. (2016) for fast ridges (~100 m maximum in ours [e.g., Figures 3(c) and (d)) vs. ~200–800 m thickness in Worman et al. (2016)). Our more pronounced scaling is in order to exploit the preserved spreading rate history of the ocean basins (so we can apply a model to different spreading rates) and to better represent observational constraints from present-day ridges and conceptual models of seafloor spreading. We also note that our scaling allows us to accommodate the different tectonic conditions present in ultraslow and slow ridges. The consequence of this is that in our model of ultraslow and slow ridges contribute 80–90% of total hydrogen production (e.g., Figures 3(e) and 5(b)) from the serpentinization of mantle peridotite at mid-ocean ridges.

Our estimates of the contribution to the hydrogen budget from OTFs (assuming width of 1 km) are roughly an order of magnitude lower than those of slow and ultraslow ridges, roughly equivalent to fast and intermediate ridges. Our present-day estimate of their contribution is ~1 • 10^{10} mol/a (0.02 Mt/a), roughly two orders of magnitude lower than those of Rüpke and Hasenclever (2017). Our 1 km estimate of the width of OTFs is almost certainly an underestimation, based on both observations at present day (e.g., Dick, 1989; Matthews et al., 2011) and numerical modeling (Rüpke & Hasenclever, 2017). Increasing the width of OTFs to 10 km (which is just above the minimum size for resolving features in global gravity data and at the lower range given by Dick (1989)) brings their contribution closer to parity with slow and ultraslow ridges (Figure 5(b)) but still an order of magnitude lower than Rüpke and Hasenclever (2017).

Our model treats OTFs as an extension of the model for MOR (i.e., the same methodology with slightly different parameter space), which is focused mainly on crustal and upper lithospheric process. Thus, we sidestep the complexity of the thermal and tectonic regimes of OTFs, their evolution through time, and their effect on lower lithosphere and mantle serpentinization. Comparably, the study of Rüpke and Hasenclever (2017) is predominantly concerned with showing how OTFs can introduce extensive volumes of fluid to the lowermost lithosphere, generating large volumes of serpentinite (and consequently, hydrogen). We consider that a better incorporation of widths into our estimates of serpentinization during

shallow lithospheric processes at fracture zones and OTFs (e.g., Matthews et al., 2011), coupled with the deeper lithosphere estimates of Rüpke and Hasenclever (2017) could provide a considerable avenue of future work for further constraining hydrogen production in ocean basins.

4.2. Integration With Plate Tectonics

We are able to describe the pulsating hydrogen fertility of ocean basins based on the tectonic and kinematic characteristics of the plates on which the basins occur. Fertile basins are located on upper plates that are not being extensively subducted along their margins while less fertile basins are characterized by being located on downgoing plates. Such kinematic evolution of the plate system, and the resulting variance in hydrogen production, occurs due to two interrelated processes pertaining to plate velocity. The first describes how plate velocity is proportional to the perimeter of a plate being subducted (Gordon et al., 1978) (Figure 7a), and the second applies to plate velocity being inversely proportional to the fraction of oceanic lithosphere on the plate (Zahirovic et al., 2015). The most poignant example of this is the Indian Ocean, which was hydrogen-infertile while the Neo-Tethys Ocean was subducting under Asia ($<1 \cdot 10^{15}$ mol/Ma [$<2 \cdot 10^{3}$ Mt/Ma] per ridge segment between 90 and 50 Ma). Once subduction ceased as Greater India started colliding with Asia at approximately 45 Ma hydrogen production increased to $>4 \cdot 10^{15}$ mol/Ma ($>8 \cdot 10^{3}$ Mt/Ma) per ridge segment. Similarly, the plates making up the Pacific Ocean during the Mesozoic and Cenozoic are almost completely devoid of continental crust, fully devoid of cratonic crust, and are (and were) being actively subducted along almost all margins. Hence, their kinematic evolution is, at times, an order of magnitude higher than the spreading rates of the Atlantic, Arctic, and Indian ocean basins (Figure 7b, c). The plates that make up these ocean basin (and in particular the Atlantic and Arctic ocean basins) all contain a large proportion of continental and cratonic lithosphere and are either not being actively subducted or have only a small portion of their perimeter being subducted (Figure 7a). The relative importance of these two drivers (perimeter proportion being subducted and proportion of continental lithosphere) can also be illustrated using the Southern Ocean, which encompasses the Australian-Antarctica plate system. Here, the Australia-Antarctica ridge separates two tectonic plates both with a large proportion of continental and cratonic lithosphere; however, the Australian plate is (and was) being actively subducted in the north under the Juva-Indonesian trench. Consequently, the spreading rate of this system over the past 40 Ma has been above 40 km/Ma (Seton et al., 2012; Whittaker et al., 2013), and our model shows that little hydrogen is produced in this ocean basin.

A third feature characterizing fertile basins is that they occur on larger tectonic plates, as opposed to smaller plates (Mallard et al., 2016) such as during the opening of the Tasman Sea (70 to 50 Ma) and formation of SE Asian microplates (15 to 0 Ma). This third feature (in addition to the aforementioned two) suggests that ocean basins formed during supercontinent breakup are the most conducive to the formation of slow and ultraslow spreading ridges and resulting fertility in hydrogen. Both plate and geodynamic modeling suggest a bimodal distribution of plate sizes through Earth history controlled by subduction geometry, wherein the preservation of large plates is ensured by convection cells in the mantle operating on 100 Ma timescales and whose size are constrained by the spacing between slabs penetrating the deeper mantle (Dal Zilio et al., 2017; Mallard et al., 2016; Matthews et al., 2016). Comparatively, smaller plates, which our model suggests produce less hydrogen, evolve more quickly over 10 Ma timescales, have a faster velocity (Schellart et al., 2007), and form in response to lithospheric stresses arising from subduction geometry (Mallard et al., 2016). Consequently, we suggest that pulses of hydrogen production from serpentinization is driven by supercontinent breakup, which results in the formation of large, slow spreading ocean basins on overriding plates.

4.3. Methane Flux

Observational data collected in situ from hydrothermal vents provide a measurement of the hydrogen-to-methane ratio being expulsed from hydrothermal systems. We employ this method after Cannat et al. (2010), as these emissions are a natural constraint to evaluate methane release in hydrothermal systems in ridge environments. At these fields, the in situ measurements suggest ratios of hydrogen to methane range between 10:1 and 1:1 (Cannat et al., 2010; Charlou et al., 2002; Kelley et al., 2005) (Figure 8). Consequently, times of elevated hydrogen generation possibly also resulted in significant methane pulses, at a maximum, up to a similar order of magnitude ($\sim 7.5 \cdot 10^{11}$ mol/a or 12 Mt/a) but more likely one magnitude lower (~1–2 Mt/a). The lower limit of methane flux suggested from this ratio is slightly higher than that of Emmanuel and Ague (2007) (hereafter, EA07) (~2.7 Mt/a or $1.6 \cdot 10^{11}$ mol/a) and than

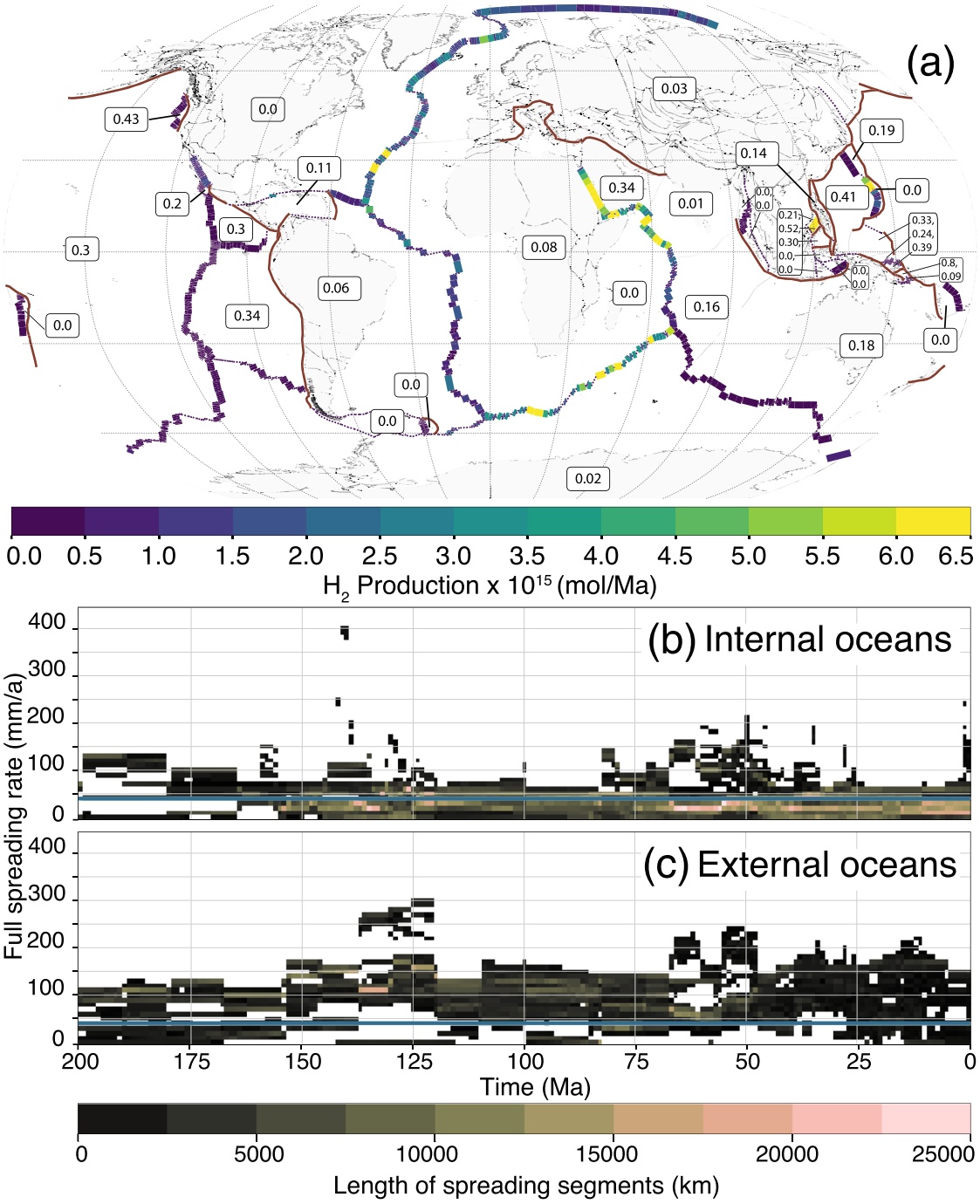

Figure 7. Summary of tectonic parameters governing H_2 system production at MORs. (a) Fraction of total plate boundary perimeter of each ocean basin that is being subducted at present day. Brown lines are subduction zones. (b) Spreading rate of internal oceans (i.e., non-Pacific oceans—Atlantic, Indian, Tethys, any back arc-basin, or marginal sea) through time. (c) Spreading rate of plates making up the Pacific Ocean Basin through time (external oceans). Blue line in both (b) and (c) represents spreading at 40 mm/a, which is the cutoff in our model for tectonic versus volcanic spreading.

that estimated by Cannat et al. (2010) of 0.4 Mt/a ($2.4 \cdot 10^{10}$ mol/a). EA07 assumed that methane was generated as a result of hydrogen production through the stoichiometric Sabatier equation; however, recent work has suggested more strongly that abiotic methane sampled at mid-ocean ridges has a deeper, mantle origin, rather than produced in the crustal column using hydrogen generated from serpentinization (e.g., Grozeva et al., 2020; Klein et al., 2019; McDermott et al., 2015; Wang et al., 2018).

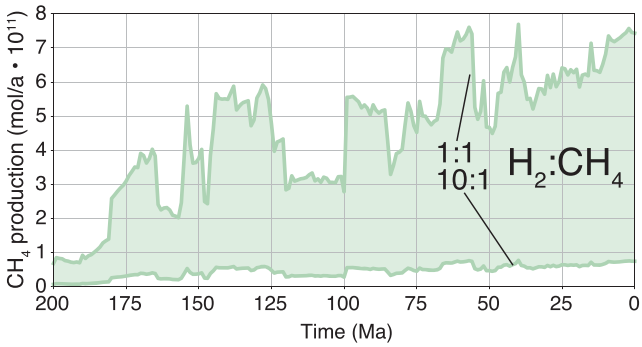

Figure 8. Range of methane flux based on observational data collected from ridges using the hydrogen-to-methane ratios— gathered from present-day hydrothermal vents—of 10:1 and 1:1 (Cannat et al., 2010; Charlou et al., 2002; Kelley et al., 2005).

The range of methane flux (~1–10 Mt/a) therefore may either have a strong or negligible impact on global methane budgets through time. Other than methane expulsed from mid-ocean ridge environments, there are global estimates for methane derived from marine hydrate deposits (2–9 Mt/a) and other "geological" sources including oceans (33–75 Mt/a) (Kirschke et al., 2013). The upper estimate of ~10 Mt/a could therefore add 10–20% to a global methane budget predominantly from just slow and ultraslow ridges, without considering the contributions from transform segments, as outlined in Rüpke and Hasenclever (2017) or a stronger contribution from faster spreading ridges, as in Worman et al. (2016). The lower estimate of our range is roughly comparable with the budget from marine hydrates but dwarfed by other sources. We expect that as more data are collected from ridge systems, a particularly interesting comparison and future step of this work will be between the values presented here (i.e., the hydrogen to methane ratio) and a methane flux that can be independently calculated using established controlling parameters.

5. Conclusions

Integration of full-plate tectonic reconstructions with geochemical models allows for the use of tectonic parameters through time and space to calculate global serpentinization volumes and the resulting hydrogen flux for the Mesozoic and Cenozoic for the first time. Our model suggests a present-day flux of $7 \cdot 10^{11}$ mol/a of hydrogen at mid-ocean ridges, driven most strongly by the evolution of slow and ultraslow spreading ridges in the Atlantic and Indian Oceans. Methane flux, estimated using in situ observations of hydrogen to methane ratios, although much more speculative than hydrogen flux, is suggested to range between ~1 and 10 Mt/a, though likely on the lower end of this range. The variation in hydrogen flux from serpentinization during the Mesozoic and Cenozoic occurs as a consequence of the breakup of Pangea. This is because Pangea breakup produced overriding, large plates with a high proportion of continental lithosphere (e.g., South American Plate and African plate) and slower seafloor spreading rates that are more likely to exhume mantle. Collectively, hydrogen and methane from serpentinization reactions at MORs worldwide evidence the fundamental tectonic control that governs global geochemical budgets through time.

Data Availability Statement

Data used and generated in the analysis is available in the Supplementary Material located at the website (https://zenodo.org/record/3571003).

Acknowledgments
Funding for this project was provided by the Deep Energy Community of the Deep Carbon Observatory. The authors thank Benjamin Tutolo for comments on an earlier version of this manuscript and Freider Klein and two anonymous reviewers for their comments that helped improve it. Suzanne Atkins is thanked for assistance with some scripts used in the analysis. Perceptually uniform color maps were used in some figures in this study to prevent visual distortion of the data (Crameri, 2018a2018a, 2018b2018b).

References

Alt, J. C., Schwarzenbach, E. M., Früh-Green, G. L., Shanks, W. C., Bernasconi, S. M., Garrido, C. J., et al. (2013). The role of serpentinites in cycling of carbon and sulfur: Seafloor serpentinization and subduction metamorphism. *Lithos*, *178*, 40–54. https://doi.org/10.1016/j.lithos.2012.12.006

Alt, J. C., & Teagle, D. A. H. (1999). The uptake of carbon during alteration of ocean crust. *Geochimica et Cosmochimica Acta*, *63*(10), 1527–1535. https://doi.org/10.1016/S0016-7037(99)00123-4

Anderson, R. N., & Nishimori, R. K. (1979). Gabbro, Serpentinite, and mafic breccia from the East Pacific. *Journal of Physics of the Earth*, *27*(6), 467–480. https://doi.org/10.4294/jpe1952.27.467

Andreani, M., Escartin, J., Delacour, A., Ildefonse, B., Godard, M., Dyment, J., et al. (2014). Tectonic structure, lithology, and hydrothermal signature of the rainbow massif (mid-Atlantic ridge 36°14′N). *Geochemistry, Geophysics, Geosystems*, *15*, 3543–3571. https://doi.org/10.1002/2014GC005269

Andreani, M., Muñoz, M., Marcaillou, C., & Delacour, A. (2013). μXANES study of iron redox state in serpentine during oceanic serpentinization. *Lithos*, *178*, 70–83. https://doi.org/10.1016/j.lithos.2013.04.008

Bach, W., & Edwards, K. J. (2003). Iron and sulfide oxidation within the basaltic ocean crust: Implications for chemolithoautotrophic microbial biomass production. *Geochimica et Cosmochimica Acta*, *67*(20), 3871–3887. https://doi.org/10.1016/S0016-7037(03)00304-1

Baker, E. T., & German, C. R. (2004). On the global distribution of hydrothermal vent fields. In C. R. German, J. Lin, L. M. Parson (Eds.), *Mid-Ocean Ridges: Hydrothermal Interactions between the Lithosphere and Oceans. Geophysical Monograph Series* (Vol. 148, pp. 245–266). Washington, DC: American Geophysical Union. https://doi.org/10.1029/148GM10

Becker, K., Sakai, H., Adamson, A. C., Alexandrovich, J., Alt, J. C., Anderson, R. N., et al. (1989). Drilling deep into young oceanic crust, Hole 504B, Costa Rica Rift. *Reviews of Geophysics*, *27*(1), 79–102.e.

Bonnemains, D., Carlut, J., Escartín, J., Mével, C., Andreani, M., & Debret, B. (2016). Magnetic signatures of serpentinization at ophiolite complexes. *Geochemistry, Geophysics, Geosystems*, *17*, 2969–2986. https://doi.org/10.1002/2016GC006321

Bown, J. W., & White, R. S. (1994). Variation with spreading rate of oceanic crustal thickness and geochemistry. *Earth and Planetary Science Letters*, *121*(3), 435–449. https://doi.org/10.1016/0012-821X(94)90082-5

Boyden, J. A., Müller, R. D., Gurnis, M., Torsvik, T. H., Clark, J. A., Turner, M., et al. (2011). Next-generation plate tectonic reconstructions. In G. R. Keller, & C. Baru (Eds.), *Geoinformatics: Cyberinfrastructure for the Solid Earth Sciences*, (pp. 95–113). Cambridge: Cambridge University Press. https://doi.org/10.1017/CBO9780511976308.008

Canales, J. P., Collins, J. A., Escartín, J., & Detrick, R. S. (2000). Seismic structure across the rift valley of the mid-Atlantic ridge at 23 20′ (MARK area): Implications for crustal accretion processes at slow spreading ridges. *Journal of Geophysical Research*, *105*(B12), 28,411–28,425. https://doi.org/10.1029/2000JB900301

Canales, J. P., Detrick, R. S., Carbotte, S. M., Kent, G. M., Diebold, J. B., Harding, A., et al. (2005). Upper crustal structure and axial topography at intermediate spreading ridges: Seismic constraints from the southern Juan de Fuca ridge. *Journal of Geophysical Research*, *110*(B12), B12104. https://doi.org/10.1029/2005JB003630

Canfield, D. E., Rosing, M. T., & Bjerrum, C. (2006). Early anaerobic metabolisms. *Philosophical Transactions of the Royal Society of London. Series B, Biological Sciences*, *361*(1474), 1819–1834; discussion 1835–6. https://doi.org/10.1098/rstb.2006.1906

Cannat, M. (1993). Emplacement of mantle rocks in the seafloor at mid-ocean ridges. *Journal of Geophysical Research*, *98*(B3), 4163–4172.

Cannat, M., Fontaine, F., & Escartín, J. (2010). Serpentinization and associated hydrogen and methane fluxes at slow spreading ridges. In P. A. Rona, C. W. Devey, J. Dyment, & B. J. Murton (Eds.), *Diversity of Hydrothermal Systems on Slow Spreading Ocean Ridges*, (Vol. 188, pp. 241–264). Washington, D. C: American Geophysical Union. https://doi.org/10.1029/2008GM000760

Cannat, M., Karson, J. A., Miller, D. J., Agar, S. M., Barling, J., Casey, J. F., et al. (1995). *Proceedings ODP, Initial Reports* (Vol. *15*). College Station, TX: Ocean drilling Program. https://doi.org/10.2973/odp.proc.ir.153.1995

Cannat, M., Mevel, C., Maia, M., Deplus, C., Durand, C., Gente, P., et al. (1995). Thin crust, ultramafic exposures, and rugged faulting patterns at the mid-Atlantic ridge (22° −24°N). *Geology*, *23*(1), 49–52. https://doi.org/10.1130/0091-7613(1995)023

Cannat, M., Rommevaux-Jestin, C., & Fujimoto, H. (2003). Melt supply variations to a magma-poor ultra-slow spreading ridge (southwest Indian ridge 61° to 69° E). *Geochemistry, Geophysics, Geosystems*, *4*(8), 9104. https://doi.org/10.1029/2002GC000480

Cannat, M., Sauter, D., Lavier, L., Bickert, M., Momoh, E., & Leroy, S. (2019). On spreading modes and magma supply at slow and ultraslow mid-ocean ridges. *Earth and Planetary Science Letters*, *519*, 223–233.

Cannat, M., Sauter, D., Mendel, V., Ruellan, E., Okino, K., Escartin, J., et al. (2006). Modes of seafloor generation at a melt-poor ultraslow-spreading ridge. *Geology*, *34*(7), 605–608.

Carlson, R. L. (2001). The abundance of ultramafic rocks in Atlantic Ocean crust. *Geophysical Journal International*, *144*, 37–48. Retrieved from. https://academic.oup.com/gji/article-abstract/144/1/37/766489

Charlou, J. L., Donval, J. P., Fouquet, Y., Jean-Baptiste, P., & Holm, N. (2002). Geochemistry of high H and CH vent fluids issuing from ultramafic rocks at the rainbow hydrothermal field (36j14VN, MAR). *Chemical Geology*, *191*, 345–359.

Charlou, J. L., Donval, J. P., Konn, C., OndréAs, H., Fouquet, Y., Jean-Baptiste, P., & Fourré, E. (2010). High production and fluxes of H2 and CH4 and evidence of abiotic hydrocarbons synthesis by serpentinization in ultramafic-hosted hydrothermal systems on the Mid-Atlantic Ridge. In P. A. Rona, C. Devey, J. Dyment, B. J. Murton (Eds.), *Diversity of Hydrothermal Systems on Slow Spreading Ocean Ridges, Geophysical Monograph Series* (Vol. 188, pp. 265–296). Washington, DC: American Geophysical Union. https://doi.org/10.1029/2008GM000752

Chen, Y. J. (1992). Oceanic crustal thickness verses spreading rate. *Geophysical Research Letters*, *19*(8), 753–756. https://doi.org/10.1029/92GL00161

Cochran, J. R., Kurras, G. J., Edwards, M. H., & Coakley, B. J. (2003). The Gakkel ridge: Bathymetry, gravity anomalies, and crustal accretion at extremely slow spreading rates. *Journal of Geophysical Research*, *108*(B2), 1480. https://doi.org/10.1029/2002JB001830

Constantin, M., Hékinian, R., Ackermand, D., & Stoffers, P. (1995). Mafic and ultramafic intrusions into upper mantle Peridotites from fast spreading Centers of the Easter microplate (south East Pacific). In *Mantle and Lower Crust Exposed in Oceanic Ridges and in Ophiolites*, (pp. 71–120). Netherlands: Springer. https://doi.org/10.1007/978-94-015-8585-9_4

Crameri, F. (2018a). Geodynamic diagnostics, scientific visualisation and StagLab 3.0. *Geoscientific Model Development* Retrieved from. https://www.geosci-model-dev.net/11/2541/2018/gmd-11-2541-2018.html

Crameri, F. (2018b). Scientific colour-maps. Retrieved from http://www.fabiocrameri.ch/resources/%2BREADME_ScientificColourmaps.pdf

Crameri, F., Conrad, C. P., Montési, L., & Lithgow-Bertelloni, C. R. (2019). The dynamic life of an oceanic plate. *Tectonophysics*, *760*, 107–135. https://doi.org/10.1016/j.tecto.2018.03.016

Dal Zilio, L., Faccenda, M., & Capitanio, F. (2017). The role of deep subduction in supercontinent breakup. *Tectonophysics*. https://doi.org/10.1016/j.tecto.2017.03.006

Dannowski, A., Grevemeyer, I., Ranero, C. R., Ceuleneer, G., Maia, M., Morgan, J. P., & Gente, P. (2010). Seismic structure of an oceanic core complex at the mid-Atlantic ridge, 22 19′ N. *Journal of Geophysical Research*, *115*, B07106. https://doi.org/10.1029/2009JB006943

Delacour, A., Früh-Green, G. L., Frank, M., Gutjahr, M., & Kelley, D. S. (2008). Sr- and Nd-Isotope Geochemistry of the Atlantis Massif (30°N, MAR): Implications for Fluid Fluxes and Lithospheric Heterogeneity. *Chemical Geology 254*(1), 19–35.

Delacour, A., Früh-Green, G. L., & Bernasconi, S. M. (2008). Sulfur mineralogy and geochemistry of serpentinites and gabbros of the Atlantis massif (IODP site U1309). *Geochimica et Cosmochimica Acta*, *72*(20), 5111–5127.

Dick, H. J. B. (1989). Abyssal peridotites, very slow spreading ridges and ocean ridge magmatism. *Geological Society, London, Special Publications*, *42*(1), 71–105. https://doi.org/10.1144/GSL.SP.1989.042.01.06

Dick, H. J. B., Lin, J., & Schouten, H. (2003). An ultraslow-spreading class of ocean ridge. *Nature*, *426*(6965), 405–412. https://doi.org/10.1038/nature02128

Dick, H. J. B., Tivey, M. A., & Tucholke, B. E. (2008). Plutonic foundation of a slow-spreading ridge segment: Oceanic core complex at Kane Megamullion, 23 30′ N, 45 20′ W. *Geochemistry, Geophysics, Geosystems*, *9*, Q05014. https://doi.org/10.1029/2007GC001645

Domeier, M., & Torsvik, T. H. (2014). Plate tectonics in the late Paleozoic. *Geoscience Frontiers*, *5*(3), 303–350. https://doi.org/10.1016/j.gsf.2014.01.002

Emmanuel, S., & Ague, J. J. (2007). Implications of present-day abiogenic methane fluxes for the early Archean atmosphere. *Geophysical Research Letters*, *34*, L15810. https://doi.org/10.1029/2007GL030532

Escartín, J., Mével, C., MacLeod, C. J., & McCaig, A. M. (2003). Constraints on deformation conditions and the origin of oceanic detachments: The mid-Atlantic ridge core complex at 15 45′ N. *Geochemistry, Geophysics, Geosystems*, *4*(8), 1067. https://doi.org/10.1029/2002GC000472

Escartín, J., Smith, D. K., Cann, J., Schouten, H., Langmuir, C. H., & Escrig, S. (2008). Central role of detachment faults in accretion of slow-spreading oceanic lithosphere. *Nature*, *455*(7214), 790–794. https://doi.org/10.1038/nature07333

Evans, B. W. (2008). Control of the products of serpentinisation by the Fe2+mg exchange potential of olivine and orthopyroxene. *Journal of Petrology*, *49*(10), 1873–1887. https://doi.org/10.1093/petrology/egn050

Fox, P. J., Schreiber, E., Rowlett, H., & McCamy, K. (1976). The geology of the oceanographer fracture zone: A model for fracture zones. *Journal of Geophysical Research*, *81*(23), 4117–4128. https://doi.org/10.1029/JB081i023p04117

Früh-Green, G. L., Plas, A., & Lécuyer, C. (1996). 14. Petrologic and stable isotope constraints on hydrothermal alteration and serpentinization of the EPR shallow mantle at Hess Deep (site 895). *Proceedings of the Ocean Drilling Program. Scientific Results Ocean Drilling Program*, *147*, 255–291. Retrieved from. https://www.researchgate.net/profile/Christophe_Lecuyer/publication/303151636_Petrologic_and_stable_isotopic_constraints_on_hydrothermal_alteration_and_serpentinization_of_the_EPR_shallow_mantle_at_Hess_Deep_Site_895/links/59e0720aaca272386b72bbbd/Petrologic-and-stable-isotopic-constraints-on-hydrothermal-alteration-and-serpentinization-of-the-EPR-shallow-mantle-at-Hess-Deep-Site-895.pdf

Früh-Green, G. L., Scambelluri, M., & Vallis, F. (2001). O–H isotope ratios of high pressure ultramafic rocks: Implications for fluid sources and mobility in the subducted hydrous mantle. *Contributions to Mineralogy and Petrology. Beitrage Zur Mineralogie Und Petrologie*, *141*(2), 145–159. https://doi.org/10.1007/s004100000228

Gordon, R. G., Cox, A., & Harter, C. E. (1978). Absolute motion of an individual plate estimated from its ridge and trench boundaries. *Nature*, *274*(5673), 752–755. https://doi.org/10.1038/274752a0

Grozeva, N. G., Klein, F., Seewald, J. S., & Sylva, S. P. (2020). Chemical and isotopic analyses of hydrocarbon-bearing fluid inclusions in olivine-rich rocks. *Philosophical Transactions of the Royal Society A*, *378*(2165), 20180431.

Gurnis, M., Turner, M., Zahirovic, S., DiCaprio, L., Spasojevic, S., Müller, R. D., et al. (2012). Plate tectonic reconstructions with continuously closing plates. *Computers & Geosciences*, *38*(1), 35–42. https://doi.org/10.1016/j.cageo.2011.04.014

Hébert, R., Bideau, D., & Hekinian, R. (1983). Ultramafic and mafic rocks from the Garret transform fault near 13°30'S on the East Pacific Rise: Igneous petrology. *Earth and Planetary Science Letters*, *65*, 107–125. https://doi.org/10.1016/0012-821X(83)90193-0

Hekinian, R., Francheteau, J., Armijo, R., Cogné, J. P., Constantin, M., Girardeau, J., et al. (1996). Petrology of the Easter microplate region in the South Pacific. *Journal of Volcanology and Geothermal Research*, *72*(3-4), 259–289. https://doi.org/10.1016/0377-0273(96)00013-3

Ildefonse, B., Blackman, D. K., John, B. E., Ohara, Y., Miller, D. J., & MacLeod, C. J. (2007). Oceanic core complexes and crustal accretion at slow-spreading ridges. *Geology*, *35*(7), 623–626.

Janecky, D. R., & Seyfried, W. E. (1986). Hydrothermal serpentinization of peridotite within the oceanic crust: Experimental investigations of mineralogy and major element chemistry. *Geochimica et Cosmochimica Acta*, *50*(7), 1357–1378. https://doi.org/10.1016/0016-7037(86)90311-X

Karson, J. A., Cannat, M., Miller, D. J., & Elthon, D. (Eds) (1997). *Proc. ODP, Sci. Results*, (Vol. 153). College Station, TX: Ocean Drilling Program. https://doi.org/10.2973/odp.proc.sr.153.1997

Kasting, J. F., & Canfield, D. E. (2012). Chapter 7: The global oxygen cycle. In A. H. Knoll, D. E. Canfield, & K. Konhauser (Eds.), *Fundamentals of Geobiology* (pp. 93–104). Oxford, UK: Wiley-Blackwell. https://doi.org/10.1002/9781118280874.ch7 Kelley, D. S., Karson, J. A., Früh-Green, G. L., Yoerger, D. R., Shank, T. M., Butterfield, D. A., et al. (2005). A serpentinite-hosted ecosystem: The Lost City hydrothermal field. *Science*, *307*(5714), 1428–1434. https://doi.org/10.1126/science.1102556

Kirschke, S., Bousquet, P., Ciais, P., Saunois, M., Canadell, J. G., Dlugokencky, E. J., et al. (2013). Three decades of global methane sources and sinks. *Nature Geoscience*, *6*(10), 813–823. https://doi.org/10.1038/ngeo1955

Klein, F., Bach, W., Humphris, S. E., Kahl, W.-A., Jöns, N., Moskowitz, B., & Berquó, T. S. (2014). Magnetite in seafloor serpentinite—Some like it hot. *Geology*, *42*(2), 135–138. https://doi.org/10.1130/G35068.1

Klein, F., Grozeva, N. G., & Seewald, J. S. (2019). Abiotic methane synthesis and serpentinization in olivine-hosted fluid inclusions. *Proceedings of the National Academy of Sciences*, *116*(36), 17,666–17,672.

Klein, F., Grozeva, N. G., Seewald, J. S., McCollom, T. M., Humphris, S. E., Moskowitz, B., et al. (2015). Experimental constraints on fluid-rock reactions during incipient serpentinization of harzburgite. *American Mineralogist*, *100*(4), 991–1002. https://doi.org/10.2138/am-2015-5112

Klein, F., Marschall, H. R., Bowring, S. A., Humphris, S. E., & Horning, G. (2017). Mid-ocean ridge serpentinite in the Puerto Rico trench: From seafloor spreading to subduction. *Journal of Petrology*, *58*(9), 1729–1754.

Konn, C., Charlou, J. L., Holm, N. G., & Mousis, O. (2015). The production of methane, hydrogen, and organic compounds in ultramafic-hosted hydrothermal vents of the Mid-Atlantic Ridge. *Astrobiology*, *15*(5), 381–399. https://doi.org/10.1089/ast.2014.1198

MacLeod, S. J., Williams, S. E., Matthews, K. J., Dietmar Müller, R., & Qin, X. (2017). A global review and digital database of large-scale extinct spreading centers. *Geosphere*, *13*(3), 911–949. https://doi.org/10.1130/GES01379.1

Mallard, C., Coltice, N., Seton, M., Müller, R. D., & Tackley, P. J. (2016). Subduction controls the distribution and fragmentation of Earth's tectonic plates. *Nature*, *535*(7610), 140–143. https://doi.org/10.1038/nature17992

Manatschal, G., Lavier, L., & Chenin, P. (2015). The role of inheritance in structuring hyperextended rift systems: Some considerations based on observations and numerical modeling. *Gondwana Research*, *27*(1), 140–164.

Matthews, K. J., Maloney, K. T., Zahirovic, S., Williams, S. E., Seton, M., & Müller, R. D. (2016). Global plate boundary evolution and kinematics since the late Paleozoic. *Global and Planetary Change*, *146*, 226–250. https://doi.org/10.1016/j.gloplacha.2016.10.002

Matthews, K. J., Müller, R. D., Wessel, P., & Whittaker, J. M. (2011). The tectonic fabric of the ocean basins. *Journal of Geophysical Research*, *116*, B12109. https://doi.org/10.1029/2011JB008413

McCollom, T. M. (2013). Laboratory simulations of abiotic hydrocarbon formation in Earth's deep subsurface. *Reviews in Mineralogy and Geochemistry*, *75*(1), 467–494. https://doi.org/10.2138/rmg.2013.75.15

McCollom, T. M., Klein, F., Robbins, M., Moskowitz, B., Berquó, T. S., Jöns, N., et al. (2016). Temperature trends for reaction rates, hydrogen generation, and partitioning of iron during experimental serpentinization of olivine. *Geochimica et Cosmochimica Acta*, *181*, 175–200. https://doi.org/10.1016/j.gca.2016.03.002

McDermott, J. M., Seewald, J. S., German, C. R., & Sylva, S. P. (2015). Pathways for abiotic organic synthesis at submarine hydrothermal fields. *Proceedings of the National Academy of Sciences*, *112*(25), 7668–7672.

Merdith, A. S., Atkins, S. E., & Tetley, M. G. (2019). Tectonic controls on carbon and serpentinite storage in subducted upper oceanic lithosphere for the past 320 ma. *Frontiers of Earth Science.*. https://doi.org/10.3389/feart.2019.00332

Meyzen, C. M., Toplis, M. J., Humler, E., Ludden, J. N., & Mével, C. (2003). A discontinuity in mantle composition beneath the southwest Indian ridge. *Nature*, *421*(6924), 731–733. https://doi.org/10.1038/nature01424

Michael, P. J., Langmuir, C. H., Dick, H. J. B., Snow, J. E., Goldstein, S. L., Graham, D. W., et al. (2003). Magmatic and amagmatic seafloor generation at the ultraslow-spreading Gakkel ridge, Arctic Ocean. *Nature*, *423*(6943), 956–961. https://doi.org/10.1038/nature01704

Miller, D. J., & Christensen, N. I. (1997). Seismic velocities of lower crustal and upper mantle rocks from the slow-spreading mid-Atlantic ridge, south of the Kane Transform Zone (MARK). In J. A. Karson, M. Cannat, D. J. Miller, D. Elthon (Eds.), *Proc. ODP, Sci. Results* (Vol. 153, pp. 437–454). Texas, USA: College Station. https://doi.org/10.2973/odp.proc.sr.153.043.1997

Minshull, T. A., Muller, M. R., & White, R. S. (2006). Crustal structure of the southwest Indian ridge at 66 E: Seismic constraints. *Geophysical Journal International*, *166*(1), 135–147. Retrieved from. https://academic.oup.com/gji/article-abstract/166/1/135/1998690

Muller, M. R., Minshull, T. A., & White, R. S. (1999). Segmentation and melt supply at the Southwest Indian Ridge. *Geology*, *27*(10), 867–870. https://doi.org/10.1130/0091-7613(1999)027<0867:SAMSAT>2.3.CO;2

Müller, R. D., Cannon, J., Qin, X., Watson, R. J., Gurnis, M., Williams, S., et al. (2018). GPlates: Building a virtual earth through deep time. *Geochemistry, Geophysics, Geosystems*, *19*, 2243–2261. https://doi.org/10.1029/2018GC007584

Müller, R. D., Sdrolias, M., Gaina, C., & Roest, W. R. (2008). Age, spreading rates, and spreading asymmetry of the world's ocean crust. *Geochemistry, Geophysics, Geosystems*, *9*, Q04006. https://doi.org/10.1029/2007GC001743

Müller, R. D., Seton, M., Zahirovic, S., Williams, S. E., Matthews, K. J., Wright, N. M., et al. (2016). Ocean basin evolution and global-scale plate reorganization events since Pangea breakup. *Annual Review of Earth and Planetary Sciences*, *44*(1), 107–138. https://doi.org/10.1146/annurev-earth-060115-012211

Niu, Y., & Hékinian, R. (1997). Spreading-rate dependence of the extent of mantle melting beneath ocean ridges. *Nature*, *385*, 326. https://doi.org/10.1038/385326a0

Oufi, O., Cannat, M., & Horen, H. (2002). Magnetic properties of variably serpentinized abyssal peridotites. *Journal of Geophysical Research*, *107*(B5), 2095. https://doi.org/10.1029/2001JB000549

Reston, T. J., & McDermott, K. G. (2011). Successive detachment faults and mantle unroofing at magma-poor rifted margins. *Geology*, *39*(11), 1071–1074. https://doi.org/10.1130/G32428.1

Rüpke, L. H., & Hasenclever, J. (2017). Global rates of mantle serpentinization and H2 production at oceanic transform faults in 3-D geodynamic models: Serpentinization at transform faults. *Geophysical Research Letters*, *44*, 6726–6734. https://doi.org/10.1002/2017GL072893

Russell, M. J., Hall, A. J., & Martin, W. (2010). Serpentinization as a source of energy at the origin of life. *Geobiology*, *8*(5), 355–371. https://doi.org/10.1111/j.1472-4669.2010.00249.x

Sauter, D., Cannat, M., Rouméjon, S., Andreani, M., Birot, D., Bronner, A., et al. (2013). Continuous exhumation of mantle-derived rocks at the southwest Indian ridge for 11 million years. *Nature Geoscience*, *6*(4), 314–320. https://doi.org/10.1038/ngeo1771

Schellart, W. P., Freeman, J., Stegman, D. R., Moresi, L., & May, D. (2007). Evolution and diversity of subduction zones controlled by slab width. *Nature*, *446*(7133), 308–311. https://doi.org/10.1038/nature05615

Seton, M., Müller, R. D., Zahirovic, S., Gaina, C., Torsvik, T., Shephard, G., et al. (2012). Global continental and ocean basin reconstructions since 200Ma. *Earth-Science Reviews*, *113*(3-4), 212–270. https://doi.org/10.1016/j.earscirev.2012.03.002

Sherwood Lollar, B., Onstott, T. C., Lacrampe-Couloume, G., & Ballentine, C. J. (2014). The contribution of the Precambrian continental lithosphere to global H2 production. *Nature*, *516*(7531), 379–382. https://doi.org/10.1038/nature14017

Shock, E. L., & Holland, M. E. (2004). *Geochemical energy sources that support the subsurface biosphere*, *Geophysical Monograph Series*, (Vol. 144, pp. 153–165). Washington DC: American Geophysical Union. https://doi.org/10.1029/144GM10

Sinton, J. M., & Detrick, R. S. (1992). Mid-ocean ridge magma chambers. *Journal of Geophysical Research*, *97*(B1), 197–216. https://doi.org/10.1029/91JB02508

Sleep, N. H., & Bird, D. K. (2007). Niches of the pre-photosynthetic biosphere and geologic preservation of Earth's earliest ecology. *Geobiology*, *5*(2), 101–117. https://doi.org/10.1111/j.1472-4669.2007.00105.x

Small, C. (1994). A global analysis of mid-ocean ridge axial topography. *Geophysical Journal International*, *116*(1), 64–84. https://doi.org/10.1111/j.1365-246X.1994.tb02128.x

Toft, P. B., Arkani-Hamed, J., & Haggerty, S. E. (1990). The effects of serpentinization on density and magnetic susceptibility: A petrophysical model. *Physics of the Earth and Planetary Interiors*, *65*(1–2), 137–157.

Torsvik, T. H., Steinberger, B., Shephard, G. E., Doubrovine, P. V., Gaina, C., Domeier, M., et al. (2019). Pacific-Panthalassic reconstructions: Overview, errata and the way forward. *Geochemistry, Geophysics, Geosystems*, *197*, 3659–3689. https://doi.org/10.1029/2019GC008402

Tucholke, B. E., Behn, M. D., Roger Buck, W., & Lin, J. (2008). Role of melt supply in oceanic detachment faulting and formation of megamullions. *Geology*, *36*(6), 455–458. https://doi.org/10.1130/G24639A.1

Tucholke, B. E., & Lin, J. (1994). A geological model for the structure of ridge segments in slow spreading ocean crust. *Journal of Geophysical Research*, *99*(B6), 11,937–11,958. https://doi.org/10.1029/94JB00338

Tucholke, B. E., Lin, J., & Kleinrock, M. C. (1998). Megamullions and mullion structure defining oceanic metamorphic core complexes on the mid-Atlantic ridge. *Journal of Geophysical Research*, *103*(B5), 9857–9866. https://doi.org/10.1029/98JB00167

Turcotte, D. L. & Morgan, J. P. (1992). Magma migration and mantle flow beneath a mid-ocean ridge. In J. Phipps Morgan, D. K. Blackman, & J. M. Sinton (Eds.). *Mantle Flow and Melt Generation at Mid-Ocean Ridges, Geophysical Monograph Series* (Vol. 71, pp. 155–182). Washington, DC.. https://doi.org/10.1029/GM071p0155

Vitale-Brovarone, A., Martinez, I., Elmaleh, A., Compagnoni, R., Chaduteau, C., Ferraris, C., & Esteve, I. (2017). Massive production of abiotic methane during subduction evidenced in metamorphosed ophicarbonates from the Italian Alps. *Nature Communications*, *8*(1), 1–13.

Wang, D. T., Reeves, E. P., McDermott, J. M., Seewald, J. S., & Ono, S. (2018). Clumped isotopologue constraints on the origin of methane at seafloor hot springs. *Geochimica et Cosmochimica Acta*, *223*, 141–158.

Whittaker, J. M., Williams, S. E., & Müller, R. D. (2013). Revised tectonic evolution of the Eastern Indian Ocean. *Geochemistry, Geophysics, Geosystems*, *14*, 1891–1909. https://doi.org/10.1002/ggge.20120

Wilson, D. S., Teagle, D. A., Alt, J. C., Banerjee, N. R., Umino, S., Miyashita, S., et al. (2006). Drilling to gabbro in intact ocean crust. *Science*, *312*(5776), 1016–1020.

Worman, S. L., Pratson, L. F., Karson, J. A., & Klein, E. M. (2016). Global rate and distribution of H2 gas produced by serpentinization within oceanic lithosphere: H2 formation in ocean lithosphere. *Geophysical Research Letters*, *43*, 6435–6443. https://doi.org/10.1002/2016GL069066

Zahirovic, S., Müller, R. D., Seton, M., & Flament, N. (2015). Tectonic speed limits from plate kinematic reconstructions. *Earth and Planetary Science Letters*, *418*, 40–52. https://doi.org/10.1016/j.epsl.2015.02.037